POLITECNICO DI TORINO

Master's Degree in Aerospace Engineering

Design, development and experimental characterization of a laboratory model for the Destiny+ Dust Analyzer (DDA)

Tutor:

Prof.ssa Sabrina Corpino

Candidate:

Marco Giuliani

October 2018

Acknowledgements

I would first like to thank my thesis supervisor Prof. Ralf Srama of the Institut für Raumfahrtsysteme - IRS at Universität Stuttgart. The door to Prof. Srama office was always open whenever I ran into a trouble spot or had a question about my research or writing. He consistently allowed this paper to be my own work, but steered me in the right direction whenever I needed it.

I would also like to thank my tutor Dr. Anna Mocker who shared with me her knowledge and ideas so that this work could come to life. Without her passionate participation and input, my thesis could have never been completed.

I would also like to acknowledge Prof. Sabrina Corpino at Politecnico di Torino as my supervisor at my home university, and I am gratefully indebted to her for her very valuable comments on this thesis.

Finally, I must express my very profound gratitude to my parents Liliana and Claudio, my sister Valentina, my grandmother Mariuccia and to my girlfriend Elisabetta for providing me with unfailing support and continuous encouragement throughout my years of study and through the process of researching and writing this thesis. This accomplishment would not have been possible without them. Thank you.

A special acknowledgement is reserved to all my friends in Alessandria, Turin and Stuttgart, people I know since many years or just a couple of months, but that have played a really important role in who I am. I could fill pages and pages with their names and the reasons why they are so important to me, but I'll just sum it up with this: thank you with all my heart for being who you are, you are irreplaceable.

Summary

This work has been developed between Politecnico di Torino and Universität Stuttgart, in the Institut für Raumfahrtsysteme (IRS).

A laboratory model for the Destiny+ Dust Analyzer (DDA) Time-of-flight (TOF) Mass Spectrometer is designed, developed and experimentally characterized. A basic and simple design is created to exploit as much as possible the cylindrical symmetry of the instrument.

Using the Software SIMION 8.1, simulations and tests are conducted to investigate the response function of the detector and to optimize the geometry and the electrical potentials applied on every component. Features of the ions after an impact ionization are studied and implemented in the simulation workbench, in order to analyse their effect on the TOF Spectrum.

Along with the linear configuration, a Reflectron setup is designed and characterized according to the size, power and mass resolution requirements: the combination of the two configurations can help having a complete understanding of the ions' angular and kinetic energy distributions.

The reason for this work is to build inside the mentioned Institute a test bench that will be used to develop the chemical analyzer flying in 2022 on the probe Destiny+. In the Introduction an overview can be found on the mission, the scientific background and the software used for the simulations, SIMION 8.1. Then the main features of our simulations are explained, along with considerations on initial kinetic energy and angular distribution, phenomena still not completely understood. The problem of the focusing of the particle beam is faced in the following chapter, while the last one is

about the Reflectron and its design.

In the Conclusions, the main results are summarized along with suggestions and comments aimed at the improvement of the system.

Contents

List of Figures

Chapter 1

Introduction

“Cosmic dust“ is the name used to identify small particles of different solid materials that exist and float in the outer space. It comprises particles that range from larger molecules with some thousands of atoms to small solid grains up to 10 μm in size (Sec. 1.2).

Dust is a really important part of the space environment: it carries information all across the universe about composition and evolution of every celestial body, as it can be comet dust, asteroidal dust, dust from the Kuiper belt or interstellar dust. Despite being in the past only an annoyance to astronomers, disturbing the sight of objects they wish to observe, in the last decades a lot of research was carried out to take advantage of it and, analysing it, finally answer to the question: what is the universe made of? Really important results were achieved and discoveries were made by missions like Cassini-Huygens by NASA, ESA and ASI (1997-2017) thanks to the Cosmic Dust Analyser (CDA), the main instrument on board.

The legacy of these missions will be taken by Destiny+ (Demonstration and Experiment of Space Technology for INterplanetary voYage Phaethon fLyby dUSt science), a mission planned for 2022 by JAXA, the Japanese Aerospace Exploration Agency, with the help of DLR (Deutsches Zentrum für Luft- und Raumfahrt e.V.) and Universität Stuttgart, represented by the IRS (Institut für Raumfahrtsysteme), that will observe and analyse dust from comets and, mostly, from the asteroid 3200 Phaethon (Sec. 1.1).

In particular, the two German institutes will develop and provide the Destiny+ Dust Analyser (DDA), that along with the Telescopic Camera for Phaethon (TCAP) and the Multiband Camera for Phaethon (MCAP) will complete the payload of the spacecraft.

With this work, a sketch of a laboratory model of the DDA was designed, simulated and experimentally characterized; in particular, this thesis regards the Time of Flight (TOF) Mass Spectrometer, the principal component of the DDA (Sec. 1.3). The software used for this work are SIMION 8.1 (Sec. 1.5), Matlab and Microsoft Excel.

1.1 Destiny+ and other missions

1.1.1 Destiny+

Destiny+ or Destiny Plus (Demonstration and Experiment of Space Technology for INterplanetary voYage Phaethon fLyby dUSt science) is a planned space mission of the Japanese space agency JAXA in cooperation with the German Space Agency DLR (Fig. 1.1). The primary goal is to test the ion propulsion on an interplanetary mission. However, scientific goals are also sought: thus, cosmic dust will be analysed and a targeted flyby on the asteroid 3200 Phaethon (Fig. 1.2) will be carried out on the body that supposedly originates the meteor stream of the Geminids.

The launch will take place in 2022 from the Uchinoura Space Center with an Epsilon rocket and the first maneuver will be to set the probe in a low Earth orbit. After few months, with the help of ion engines, the orbit will continue to raise for a total of 1.5 years. A flyby on the moon will then accelerate the probe into an interplanetary orbit. On the further flight it is hoped to analyse interplanetary as well as cosmic dust. In addition, fly-bys on some near-Earth objects, especially the asteroid 3200 Phaethon are planned after a flight time of 4 years. After that, the ion engines will still have fuel for orbit corrections and to possibly fly to other destinations.

Destiny+ will be equipped with thin film solar cells and modern temperature control sensors. Its position control system is designed to be as compact as possible. The spacecraft is provided with a protective aluminium shield, so that it can withstand radiation exposure up to 30 krad.

The spacecraft is powered by four μ10 solar electric ion engines, as used in the Hayabusa and Hayabusa 2 probes. Destiny+, unlike its predecessors, will use for the first time all four engines simultaneously. The engines deliver a total thrust of 40 mN at a power of 1670 W, which accelerates the probe by 83 $\mu\mathrm{m}/s^2$. The mass of the engines (without the Xenon fuel) is 59 kg.

To date, active asteroids have been little explored. They are the link between inactive asteroids and active comets. The relatively short distance between Phaethon and the sun (only 0.14 astronomical units) leads to high temperatures on the surface of the asteroid, such that high amounts of gas and dust are generated. The larger dust particles are spread along Phaeton's orbit and each year the Earth passes this debris belt leading to the well known meteor shower of the Geminids. Phaethon has already lost most of its volatile material and only little activity can be detected today. Nonetheless, due to this activity, Phaeton is classified as an active asteroid. [1]

The payload will consist of three main instruments:

- the Destiny+ Dust Analyzer (DDA) will be provided by the DLR and built by the University of Stuttgart;
- the Telescopic Camera for Phaethon (TCAP), that has a mass of 15.8 kg;
- the Multiband Camera for Phaethon (MCAP), a spectroscopic camera that weighs 3.5 kg and examines light in the wavelengths 390 nm, 550 nm, 700 nm and 850 nm.

During the quick flyby at 25 km/s, remote sensing and *in situ* observations will be carried out by Destiny+ and the results promise to improve our understanding of the Solar System. The MCAP will characterize the 6 km-class object from afar and the dust sensor developed at the University of Stuttgart will analyse the surrounding dust cloud along Destiny+'s trajectory. Before the spacecraft reaches the asteroid, exact measurements of the interplanetary and interstellar dust environment will be carried out. Of special interest are the elemental composition of the fine interstellar grains and their interaction with the heliosphere. Destiny+ and DDA thereby establish a bridge between the planetary sciences and astrophysics.

Germany has gained important competencies in the field of space sensor technologies in recent years, especially through Cassini's Cosmic Dust Analyzer (CDA) project. Destiny+ is the University of Stuttgart's next meaningful project in this field. Under the leadership of Dr. Ralf Srama at the University of Stuttgart's Institute of Space Systems (IRS), preparations are being made for the development of the new space telescope. [1]

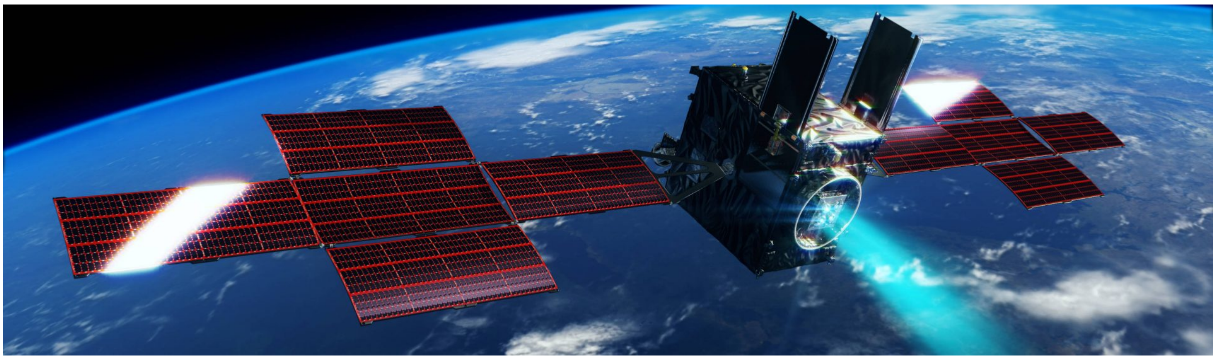

Figure 1.1: Destiny+ Spacecraft, artist's impression. [2]

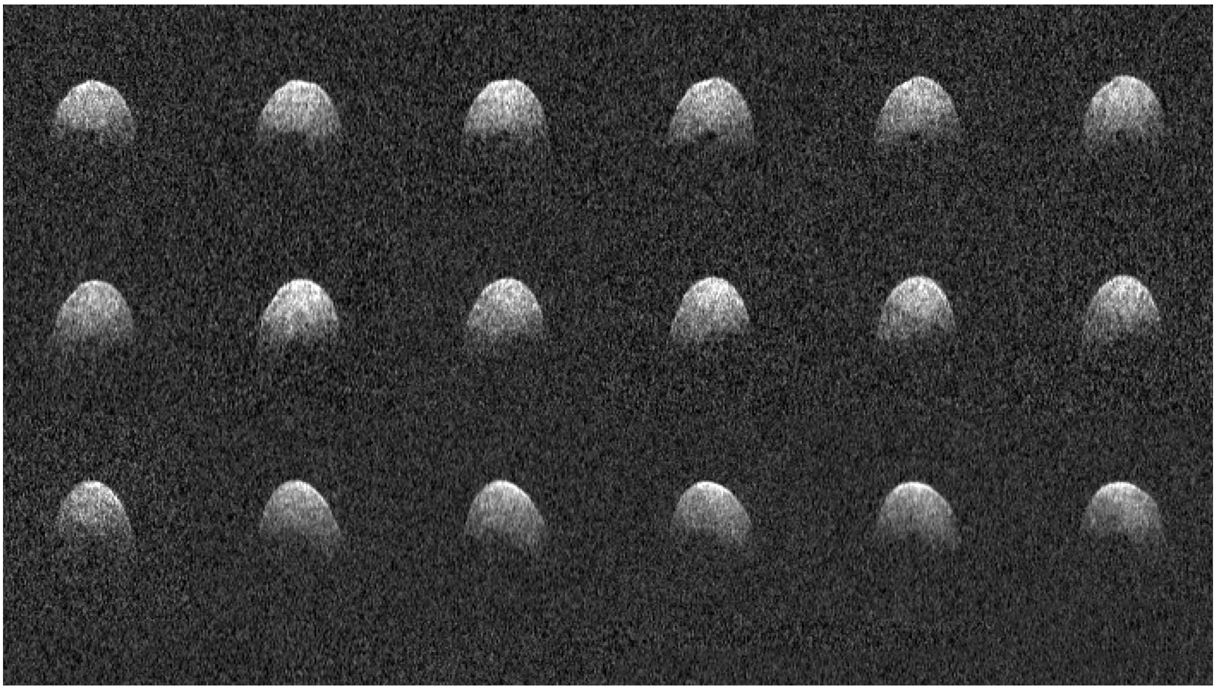

Figure 1.2: Radar images of near-Earth asteroid 3200 Phaethon generated by astronomers at the National Science Foundation's Arecibo Observatory on Dec. 17, 2017. Observations of Phaethon were conducted at Arecibo from Dec. 15 through 19, 2017. At time of closest approach on Dec. 16 at 3 p.m. PST (6 p.m. EST, 11 p.m. UTC) the asteroid was about 6.4 million miles (10.3 million kilometers) away, or about 27 times the distance from Earth to the moon. The encounter is the closest the asteroid will come to Earth until 2093. Image credit: Arecibo Observatory/NASA/NSF [3]

1.1.2 Past and Future Missions

In the past five decades, dust detectors on various spacecraft have succeeded supremely in teaching us about our solar system dust environment. The detectors aboard Galileo and Ulysses improved our knowledge of the mass distribution of the interplanetary dust particles [4] [5], and detected an interstellar dust stream that penetrates our solar system [6]. The Galileo dust detector measured dust clouds around Jupiter's Galilean satellites [7] and with other measurements it was concluded that Io's volcanoes are the source of dust streams in the Jovian system. Integrated time-of-flight mass spectrometers on board the Vega and Giotto spacecraft analysed cometary dust particles [8] [9] and suggested evidence of organic compounds [10]. [11]

Future missions, like Destiny+, are already planned: the Europa Clipper mission, planned for launch between 2022 and 2024, will explore the Jupiter's moon Europa and measure the composition of small, solid particles ejected from it. The spacecraft will be equipped with the SUrface Dust Analyser (SUDA), a time-of-flight, reflectron-type impact mass spectrometer (Fig. 1.3), optimised for a high mass resolution which only weakly depends on the impact location [12]. This spectrometer has heritage from the Cassini CDA (Fig. 1.4) and the Stardust CIDA (Fig.1.5) instruments and its concept was the inspiration for the realization of the DDA.

The reflectron configuration was chosen because it can significantly reduce the effect on the initial energy spread on the mass resolution, even if it is supposed to be far lower than a laboratory laser-ionization reflectron. For this reason the retarding field was optimized to achieve the best spatial and time focusing at the ion detector area in the center of the instrument. A full-size prototype was built in order to demonstrate its performance (Fig. 1.6) through calibration experiments at the dust accelerator at NASA's IMPACT institute at Boulder, CO with a variety of cosmochemically relevant dust analogues [12].

1.2 Cosmic Dust

Also known as extraterrestrial dust or space dust, cosmic dust is basically the origin of every planet or star in the universe. All these tiny particles floating around

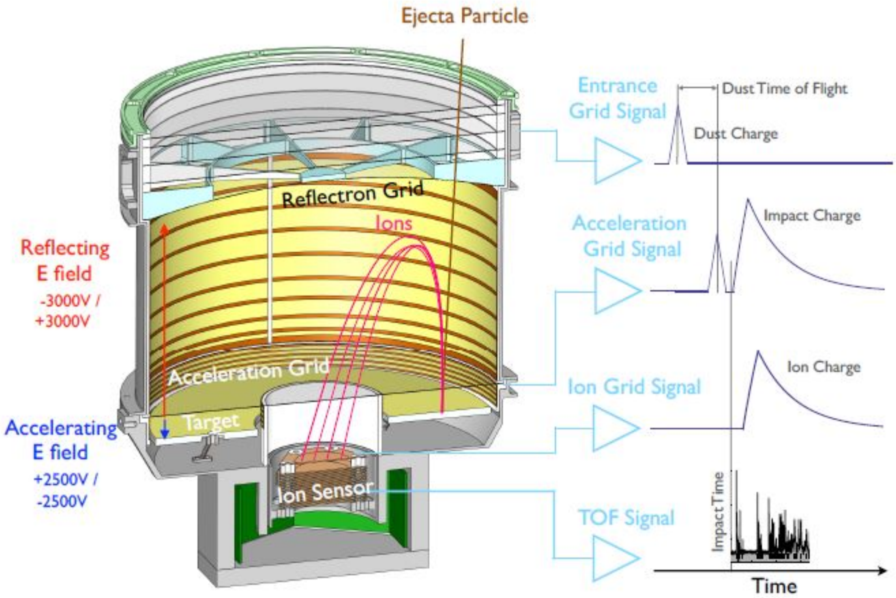

Figure 1.3: Function principle of the SUDA impact mass spectrometer. [12]

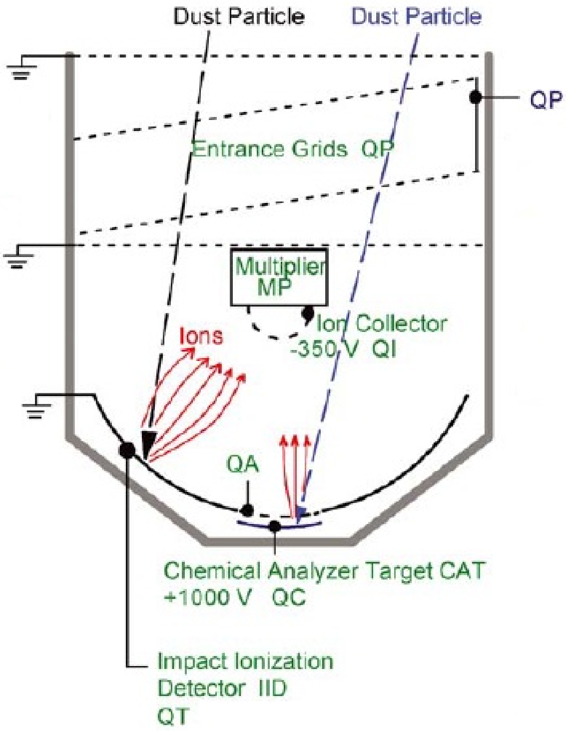

Figure 1.4: Sketch of the working principle of CDA. Dust particles pass through the entrance grids generating the signal QP (primary charge); depending on their impact on the instrument, the signal QC (chemical analyzer target), QT (impact ionization detector) or QA (chemical analyzer grid) is generated with different shapes. After the impact, the ions are accelerated towards the detector that acts as a multiplier. [13]

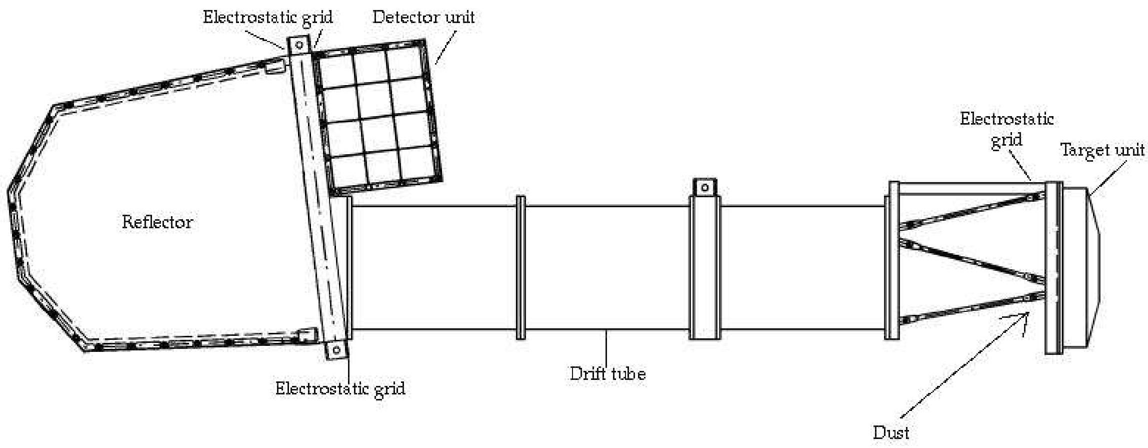

Figure 1.5: Cometary and Interstellar Dust Analyser (CIDA). [14]

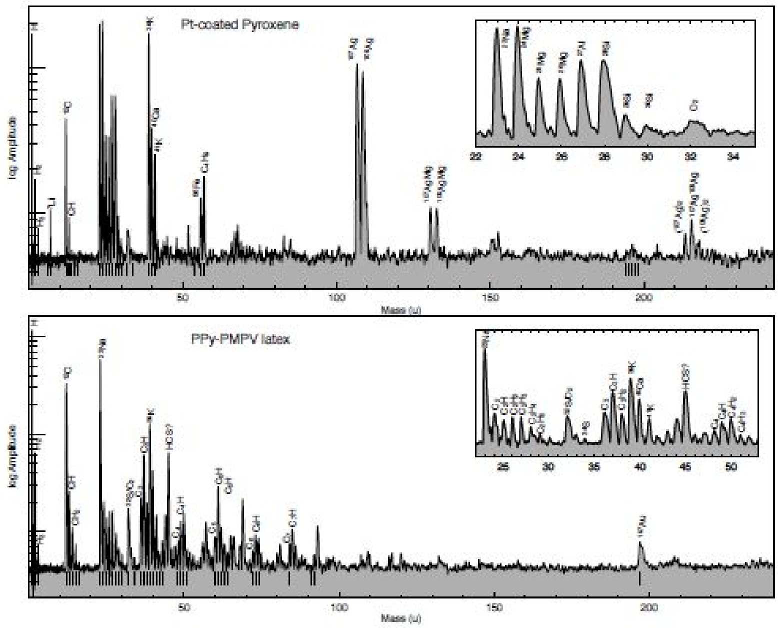

Figure 1.6: Example spectra of a pyroxene particle impact on a silver target and of a latex particle on a gold target recorded with SUDA. [12]

in the space, when subject to gravitational fields, can gather and form a discrete mass that generates step by step stronger gravitational forces, attracting more and more dust: thus a celestial body is born. But dust is not all the same: the main differences are in terms of size, material and origin. The size of these particles can vary from collections of a few molecules up to large grains 0.1 mm long (Fig. 1.7). The material and the origin of dust are closely related, since depending on the star or comet that produced it, the composition will be different.

As shown in Fig. 1.8, dust is formed in stars and is then spread in space by star wind or a massive star explosion (Supernova). The dust is then 'recycled' in the clouds of gas and some of it is consumed as formation material for the new generation of stars. When astronomers started looking into space with infrared cameras, they discovered that the in the past annoying cosmic dust is actually very interesting and important to lots of astronomical phenomena. The light reflected and refracted by dust is at longer wavelengths compared to the absorbed starlight. Astronomers can see the shine of dust using special instruments for the far-infrared and submillimetre part of the electromagnetic spectrum. Its analysis can reveal information about phenomena like the formation of the Solar System: here, dust also plays a major role in the zodiacal light, Saturn's B Ring spokes, the outer diffuse planetary rings at Jupiter, Saturn, Uranus, Neptune and comets.

Cosmic dust can be detected by indirect methods that exploit the radiative properties of particles or it can also be detected directly (*in situ*) using many different collection methods and from many different collection locations. In interplanetary space, dust detectors on planetary spacecraft have been built and flown and some are presently being built to fly. The large orbital velocities of dust particles in interplanetary space (typically 10–40 km/s) make intact particle capture problematic; the impact speed of a dust particle in space depends on its heliocentric speed and on the spacecraft trajectory [11]. Instead, *in situ* dust detectors are generally designed to measure parameters associated with the high-velocity impact of dust particles on a target in the instrument, and then derive physical properties of the particles (like mass and velocity) through laboratory calibration. Over the years dust detectors have measured, among others, the impact light flash, acoustic signal and impact

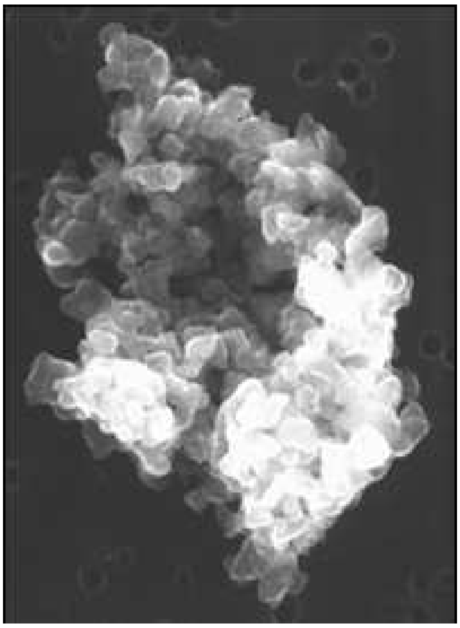

Figure 1.7: Cosmic dust grain 11 microns in diameter. [15]

ionization (Sec. 1.4). Time-of-flight Mass Spectrometry is a method used for *in situ* dust measurements that can provide information about quantity, charge and mass of the particles.

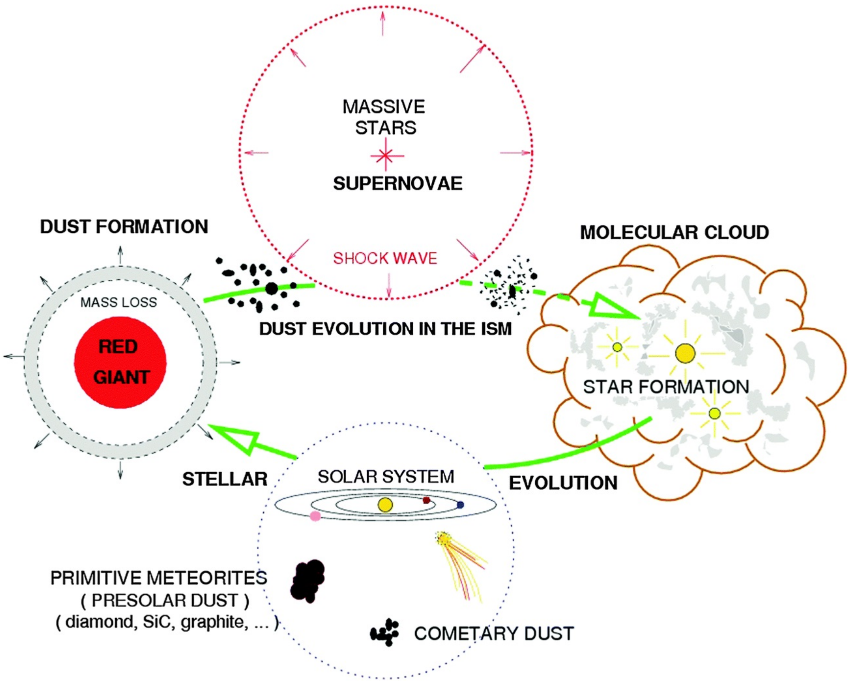

Figure 1.8: A schematic view of the interstellar dust lifecycle. Dust is principally formed around the asymptotic giant branch (AGB) and red giant (RG) 'evolved' stars and also, to some less well-characterised extent in supernova remnants. At the end of its life it is incorporated into young stars in molecular clouds and, eventually, into comets, asteroids and planets. Throughout this cycle the dust properties evolve through energetic collisions with the gas and grains in supernova-generated shock waves and also through the effects of UV-irradiation. Reproduced from A. P. Jones, Ref. [16]. [17]

1.3 TOFMS

Time-of-flight Mass Spectrometry (TOFMS) is a method of mass spectrometry in which an ion's mass-to-charge ratio is determined via a time of flight measurement. Ions are created and then accelerated by an electric field. Because of this acceleration, every ion having the same charge will have the same kinetic energy too. The velocity of the ion depends on the mass-to-charge ratio (heavier ions with the same charge can reach lower speeds, lighter ions or with higher charge will be faster). The time (Time of flight, TOF) that it takes for the ion to reach a detector at a known distance is measured: this time will depend on the velocity of the ion, and therefore is a measure of its mass-to-charge ratio. Knowing this ratio and the expected charge, one can calculate the mass and identify the ion.

An early time-of-flight mass spectrometer, called the "Velocitron", was reported by A. E. Cameron and D. F. Eggers Jr, working at the Y-12 National Security Complex, in 1948. The idea had been proposed two years earlier, in 1946, by W. E. Stephens of the University of Pennsylvania in a meeting at the Massachusetts Institute of Technology of the American Physical Society [18]. Since then, TOFMS has been largely used in chemistry laboratories (Fig. 1.11) along with other types of spectrometers especially to discover the composition of organic compounds and to analyse water resources [19] thanks to its high transmission, robustness and ability to record the whole mass spectrum quasi simultaneously [20]. Usually in laboratories ions are created by pulsating laser beams on the particles to be examined: the energy absorbed by the laser is high enough to start the dissociation of the particles in anions and cations, so they can be accelerated in opposite directions by the electric field.

If the spectrometer is part of the payload of a scientific spacecraft, the high orbital velocities of cosmic dust particles can be converted by an impact into energy for the dissociation: this process is called impact ionization (Sec. 1.4). This holds pros and cons: on one hand, the ionization is totally passive, so electrical power is only needed for the accelerating fields and the detectors; on the other hand, the impact cannot be controlled, so the trajectory of the ions bouncing off the target is highly influenced by the initial kinetic energy and the direction in terms of angles. Other two drawbacks are that the electric power, so the intensity of the accelerating field, is limited on board and that ejecta from the target will be detected as well together with the ions. Moreover, regarding the TOF mass spectrometer itself, it has a relatively poor mass resolution due to the spread in the initial thermal energies or velocity of the ions with the same mass-to-charge ratio as well as to the spatial distribution of them within the ionization region [21]. To reduce and minimize the effects of velocity distribution on time resolution, several methods were successfully introduced, such as delayed pulse extraction [22], reflectrons (Fig. 1.10) [23], electrostatic sectors [24] [25], orthogonal acceleration [26] and multiturn ion optical geometries [27].

After the ionization, the particles possess a certain electric charge q. The potential energy of a charged particle in an electric field is related to the charge of the particle and to the strength of the electric field:

$$E_P = qV \tag{1.1}$$

where E_P is the potential energy, q is the charge of the particle, and V is the electric potential difference, that is to say the voltage. When the charged particle is accelerated into the time-of-flight tube by the voltage V, its potential energy is converted to kinetic energy. The kinetic energy of any mass is:

$$KE = \frac{1}{2}mv^2 \tag{1.2}$$

Since the potential energy is converted into kinetic energy, it means that equations 1.1 and 1.2 are equal

$$qV = \frac{1}{2}mv^2 \tag{1.3}$$

The velocity of the charged particles after acceleration will not change since it moves in a field-free time-of-flight tube, called drift zone. This distance is one of the most important parts of the instrument, because here particles are filtered according to their velocity, and thus to their mass-to-charge ratio. The average velocity of the particle can be determined in a time-of-flight tube by the length of the path (x) of the flight of the ion and the time of the flight of the ion (t), that can be measured. Thus,

$$v = \frac{x}{t} \tag{1.4}$$

and substituting equation 1.4 into 1.3, we obtain:

$$qV = \frac{1}{2}m\left(\frac{x}{t}\right)^2 \tag{1.5}$$

Rearranging 1.5 so that the time of flight is expressed by everything else:

$$t^2 = \frac{x^2}{2V}\frac{m}{q} \tag{1.6}$$

Applying the square root to both members,

$$t = \frac{x}{\sqrt{2V}}\sqrt{\frac{m}{q}} \tag{1.7}$$

These factors for the time of flight have been grouped on purpose. $\frac{x}{\sqrt{2V}}$ contains constants that in principle do not change since geometry and voltages are fixed. Equation 1.7 can thus be written as

$$t = k\sqrt{\frac{m}{q}} \tag{1.8}$$

where k is a proportionality constant representing factors related to the instrument settings and characteristics. Equation 1.8 reveals more clearly that the time of flight of the ion varies with the square root of its mass-to-charge ratio. If the charge is supposed to be the same among all ions, the same relation can also be written as

$$t = b + a\sqrt{m} \tag{1.9}$$

where the shift parameter b represents any time offsets between the trigger and the start of the spectrum due to the production process of the ions. The stretch parameter a is determined by the physical setup of the instrument. Since the ions tested in previous experiments have on average a single charge and thus the mass of the dust particle and the ion are the same except for the negligible mass of an electron, in this work, especially for the simulations, it will usually be referred to ions also as ”particles”.

The TOF Mass Spectrometer here studied can be sketched as in Fig. 1.9: the particles impact at hypervelocity speed on the target, typically made of Rhodium, that is at a certain positive voltage, and ions are here created. A grounded grid a few cm in front of the target provide a steep voltage gradient: this is how an electric field of intensity E is created

$$\vec{E} = -\nabla V \tag{1.10}$$

This electric field induces in the ions an acceleration

$$a = \frac{qE}{m} \tag{1.11}$$

in such a way that electrons and negative ions are pushed again against the target, while positive ions fly in the other direction towards the detector. A second grounded and shielding grid, before the detector, delimits the drift zone, the distance in which the acceleration of the ions is null. Here the velocity gained during the acceleration becomes fundamental: faster ions will get to the second grid in less time compared to the slower ones and the longer this distance is, the more the ions will be sorted. This results in a higher resolution of the instrument, since in the produced spectrum peaks of elements with different masses will be more distant one from another and easier to distinguish. After the second grid, the detector at a certain negative voltage will provide a second short acceleration zone and will produce an electric signal proportional to the number of detected particles. The signal produced by the impact on the target activates a trigger that start the measurement of the TOF, and as seen before the TOF is used to calculate the mass-to-charge ratio.

The target is a small metallic plate, the material is chosen according to chemical properties and elemental mass: a good choice is Rhodium, since it is not reactive with the usual dust used in experiments and its atomic mass, of around 100 amu, is much greater than the elements found in space and so recognizable in the spectra. The grids, though during the simulations they were supposed as ideal (Chap. 2), have a limited transmission which usually is about 90%, sometimes up to 95%; because of this, some of the flying ions will be impact the grids and never reach the detector. The chosen detector is a Micro-Channel Plate (MCP) detector (Fig. 1.12). An MCP is a wedge made from highly resistive material typically 2 mm thick with a regular array of tiny tubes or slots (microchannels) leading from one face to the opposite, densely distributed over the surface. The microchannels are typically around 10 μm in diameter (6 μm in high resolution MCPs) and spaced apart by approximately 15 μm; they are parallel to each other and enter the plate at a small angle to the surface (8° from normal). Because of this angle, a particle or photon that enters one of the channels is guaranteed to hit the wall: the impact starts a cascade of electrons that propagates through the channel, amplifying the original signal by several orders of magnitude depending on the electric field strength and the geometry of the micro-channel plate. This process is fundamental because single ions flying into the detector produce an electric signal too small to enable their direct detection. After the cascade, the electrons exit the channels

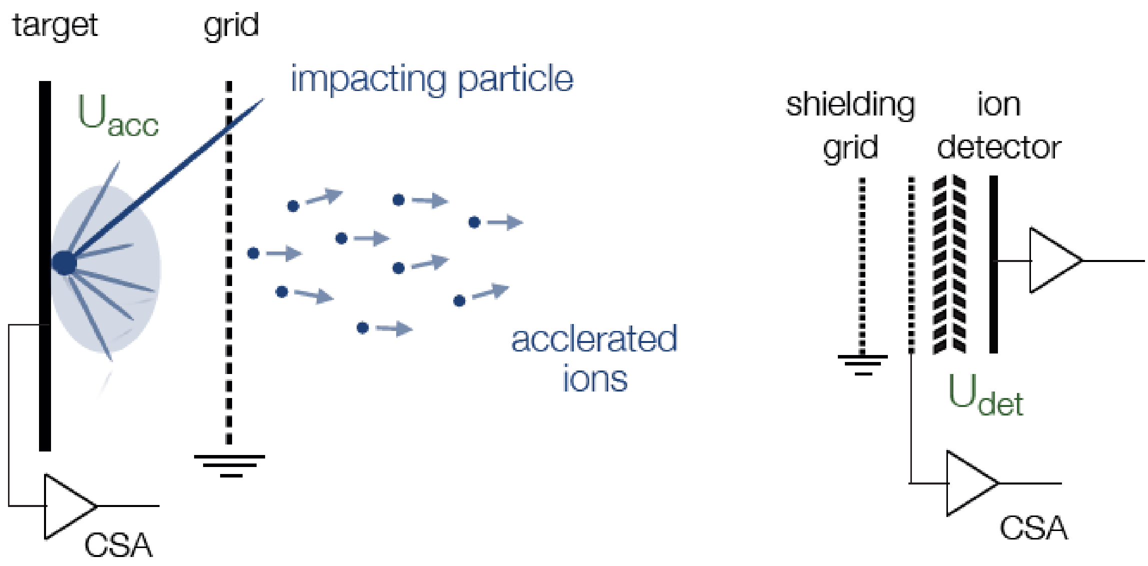

Figure 1.9: The schematic drawing of the BERTA time-of-flight mass spectrometer: the potentials on the target and the detector are indicated as U. [28]

on the opposite side of the plate where they are collected on an anode, where the signal is generated. Research and technology allowed scientists to give birth to more modern and effective MCPs, like Dual (Fig. 1.13), Chevron and Z stack MCPs.

The full experimental setup, of which the TOF Mass Spectrometer is just the final part, is shown and explained in Fig. 1.14.

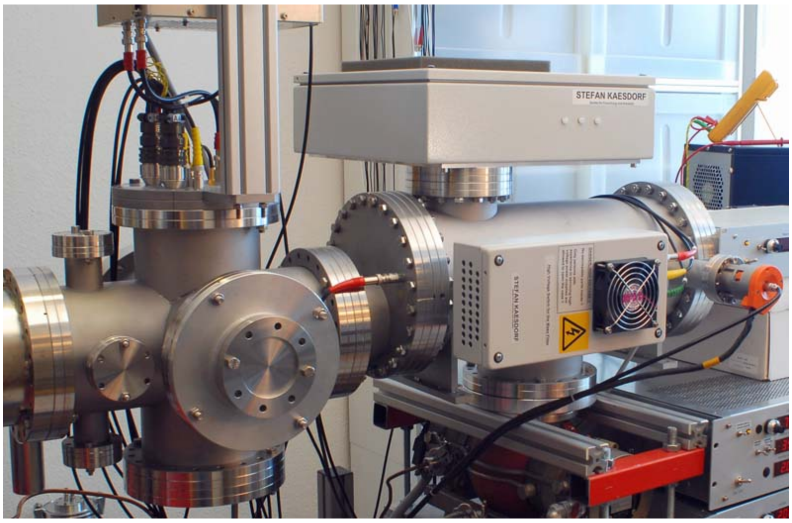

Figure 1.10: Orthogonal extraction reflectron time-of-flight spectrometer OFT12, overall length ca. 900 mm, angle between in- and outgoing ion beam ca. 8°, field free drift length ca. 900 mm, two-stage ion reflector for second order energy focusing. [29]

Figure 1.11: TripleTOF® 6600 Quadrupole Time-Of-Flight (QTOF) mass analyzer. [30]

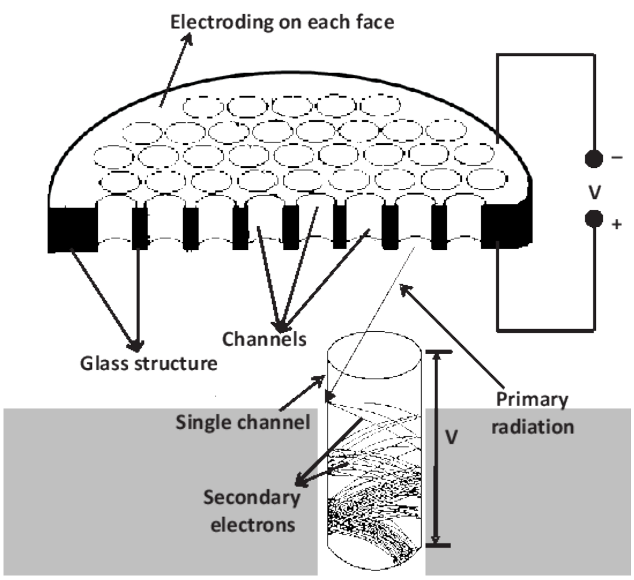

Figure 1.12: Schematic and working principle of a micro channel plate detector (MCP). [31]

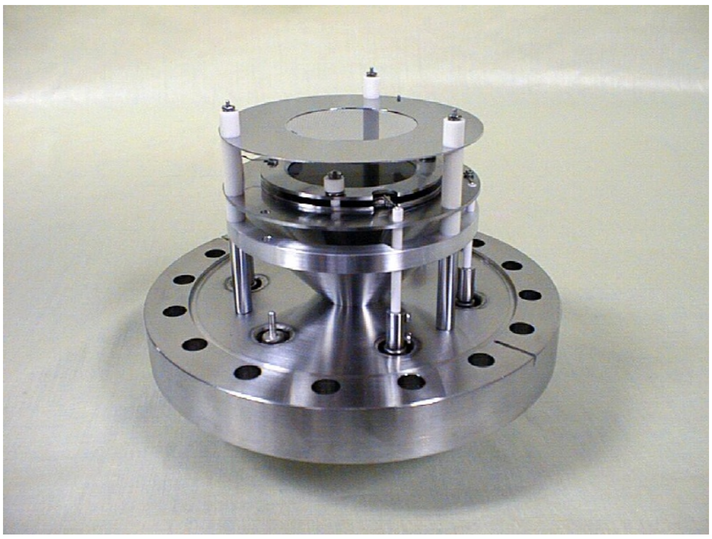

Figure 1.13: 40mm MCP Dual Detector on 6 Inch Conflat Flange. [32]

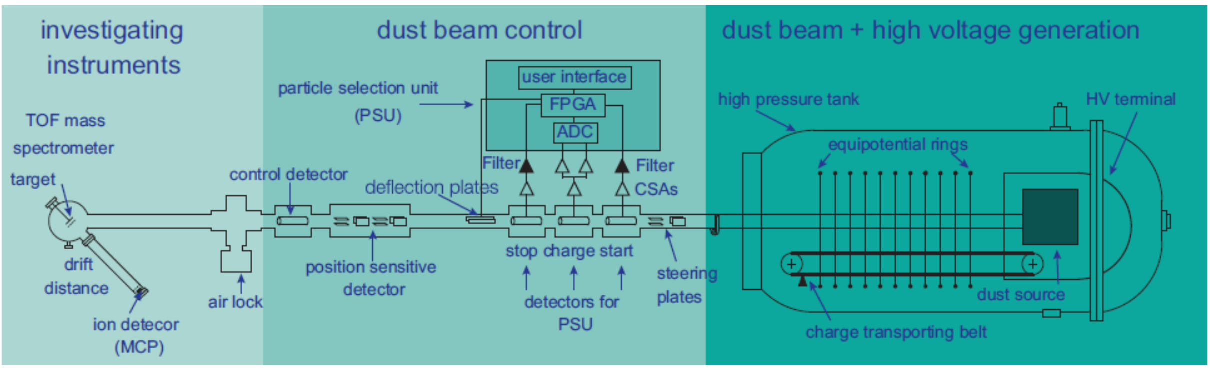

Figure 1.14: Overview of the experimental set up: the dust particles are charged in the dust source, passed into an accelerating electrostatic field of about 2 MV (right) and focused towards an investigating instrument, in this case a linear TOF mass spectrometer (left). Before reaching the instrument, the particles are registered, characterized, and eventually selected while passing the beam line detectors of the Particle Selection Unit (PSU) (center). [28]

1.4 Impact Ionization

By definition, impact ionization is the process in a material by which one energetic charge carrier can lose energy by the creation of other carriers. For example, in semiconductors, an electron with enough kinetic energy can knock a bound electron out of its state and promote it to a state in the conduction band. In order to give carriers sufficient kinetic energy, a sufficiently large electric field must be applied, in essence requiring a sufficiently large voltage. If this occurs in a region of high electrical field, then it can result in avalanche breakdown (Fig. 1.16). This process is exploited in avalanche diodes, by which a small optical signal is amplified before entering an external electronic circuit. In an "avalanche photodiode" the original charge carrier is created by the absorption of a photon [33].

For decades the interaction of micron and sub-micron sized particles with a solid surface at velocities near or exceeding the speed of sound in the materials at question has been used for the *in situ* detection and characterization of cosmic dust particles. A fast particle impacting a solid surface causes mechanical stress in the particle and the target body, generating compression and even shock waves depending on the impact velocity. This is used by a large number of dust detector types. The methods yielding the highest sensitivity for detection of dust particles in space rely on impact ionization:

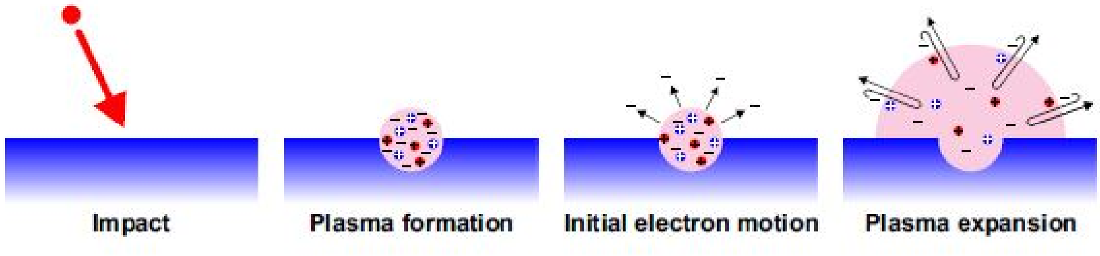

Figure 1.15: Depiction of the plasma generation and expansion process due to hypervelocity impact. [34]

when a dust particle impacts a solid target, parts of the impactor and the target are vaporized and ionized by the energy released during the impact. This leads to the formation of an impact plasma (Fig. 1.15), expanding rapidly into the surrounding vacuum. The constituents of the plasma are separated by an electrostatic field, and depending on their polarity, accelerated towards either an ion detector or back the target plane. The generated charge signals are then amplified and recorded. With suitable charge detectors and instrument geometry, impact ionization sensors can act as highly sensitive time-of-flight (TOF) mass spectrometers. [28]

The advantages of such detectors are their simplicity (the ion generation is passive, except for the particle acceleration) and the possibility of measurements of the dynamical properties of the particle and its chemical composition at the same time, as well as the reduction of noise because of coincidence detection. These methods can give insights into various aspects of the processes caused by hypervelocity impacts, like the thermodynamic properties of the ions or the temperature of the plasma cloud. In addition to the development, calibration, and testing of instruments dedicated to the investigation of dust particles in space, hypervelocity impact experiments provide an opportunity to obtain a better understanding of the impact process itself and to study matter under extreme conditions, i.e. high pressures and temperatures.

One of the models that most successfully described the process of impact ionization is given by [28].

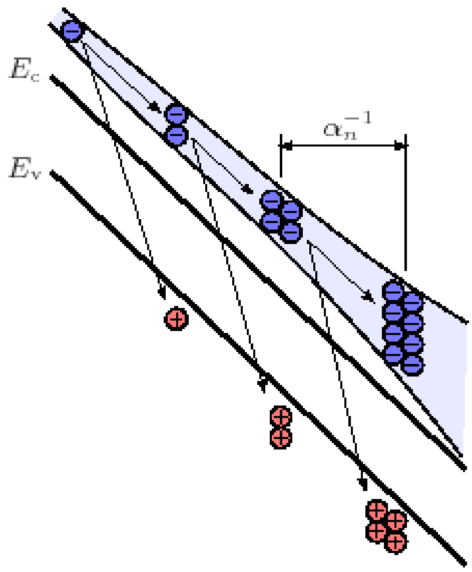

Figure 1.16: Symbolized process of a pure electron induced impact-ionization avalanche generation. After an electron is accelerated along an average distance α_n^{-1} it undergoes a collision and the excess energy produces a new electron-hole pair. Consecutive collisions can trigger an avalanche. [33]

1.5 SIMION

"SIMION Version 8.1 is a software package primarily used to calculate electric fields and the trajectories of charged particles in those fields when given a configuration of electrodes with voltages and particle initial conditions, including optional RF (quasistatic), magnetic field, and collisional effects. In this, SIMION provides extensive supporting functionality in geometry definition, user programming, data recording, and visualization. It is an affordable but versatile platform, widely used for over 30 years to simulate lens, mass spec, and other types of particle optics systems." [35]

Despite being a very specific and technical software, it is also really flexible (Fig. 1.17) and with high computing capabilities. For this work, it was used to simulate the trajectories of ions flying in the studied TOF Mass Spectrometer. The main environment in SIMION in which it is possible to work, it's the Workbench. The Workbench is actually the representation of the real system that has to be simulated, and contains the single components and their geometry, their position in the space, the electric or magnetic field applied to them, the particles that have to be flown and their features. The various components and electrodes are defined in the software as "potential arrays": they are basically arrays and matrices of defined points that will determine the geometry of the electrode (Fig. 1.18) and its volume in the space (Fig. 1.19). A single potential array can represent just an electrode or a whole component made of more electrodes; the user has to properly create these arrays according to the final design and its properties.

Lua is the main programming language supported in and embedded inside SIMION 8. Lua suits SIMION well for its efficiency, its simplicity, its small size, its flexibility and its data definition capabilities (Lua is even used as the basis for the new FLY2 format). Lua programs (unlike SL ones) do not need to be compiled but rather can be run directly in SIMION. This language can interface to other programs or programming languages via a simple os.execute call or LuaCOM, which is used in one of the SIMION examples to control Excel from SIMION. The SIMION batch-mode capabilities offer a Lua interface as well (based on the command-line interface) [36]. The potential arrays too can be generated starting from "geometry files" written in Lua language, that define the total size of the array, the actual geometry of electrodes and their position in the array. Every array can be subsequently rescaled and repositioned inside the Workbench. The geometries can also be imported by CAD designs created with more suitable programs (Fig. 1.22).

The main functions of the Workbench are:

- to define all the boundary conditions for the flight of the ions, i.e. the geometry of the system and the electric and/or magnetic fields;
- to choose how many ions will be flown and their initial properties;
- to choose the recording parameters for the flight data;
- to set the electric potential to every electrode;
- to fly the ions and print or produce the log file with the data chosen previously.

Other optional functions are available for an easier understanding of the system, like for example the displaying of the magnetic or electric field lines. Once the particles are flown, the log file is used for studying their behaviour during the flight. The software is also displaying every trajectory (both as lines or as flying dots) during the flight (Fig. 1.20): if something was not defined correctly, it can be noticed immediately from the picture. Really useful can also be the function for visualizing the Potential Energy (PE) surfaces that show the electric fields as 3D surfaces (Fig. 1.21).

The log file is then imported in another software like Matlab or Excel. In this work, this programs were used for analysis on the detection, displaying of spatial distributions and creation of mass and TOF spectra. Results from previous flights can then be used as inputs for new simulations. Please note that the log can be produced in a verbose format, where every parameter has an alphabetic tag as explanation, or in a delimited one, where only strings of numbers separated by commas are printed. Here parameters are defined by their position in the string and by their value. The "verbose" format is easier to understand, useful to take a quick look at the results; the "delimited" one is better for being imported and processed, since there are no alphabetic characters except for delimiters in each line.

In SIMION, electric fields can be modelled as boundary value problem solutions of the Laplace equation, an elliptical partial differential equation. The specific method used within SIMION to solve this equation is a finite difference method called over-relaxation. This technique is applied to a three-dimensional potential array. The Laplace equation has the convenient property that its solution is a sum over the contribution from each electrode. Therefore, after the electric field array has been found once by iteration, the voltages of the individual electrodes can be changed and the new fields are immediately obtained. The objective is to obtain a best estimate of the voltages for the points between the electrodes. The three-dimensional array is chosen to have either cylindrical, planar or no symmetry at all.

When the electric fields have been obtained, the trajectories of charged particles in these fields are calculated. Particle trajectory calculations are a result of three interdependent computations. First, electrostatic forces are calculated at the current ion position: these are then used to compute the current ion acceleration and then, by numerical integration techniques, to predict the position and velocity of the ion at

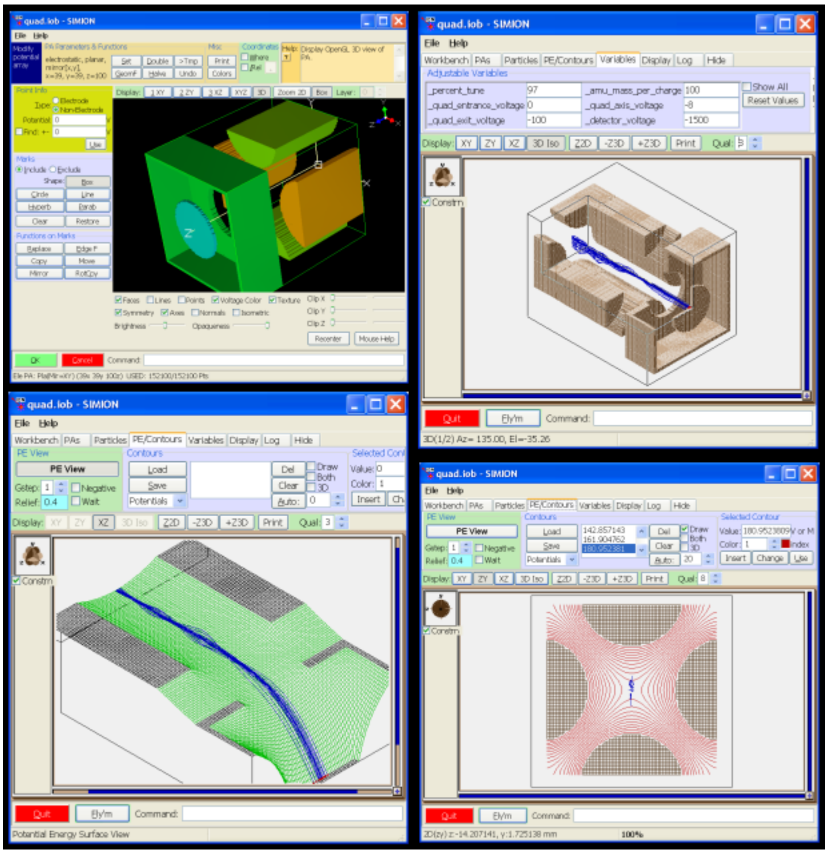

Figure 1.17: Screenshots above show model, field, and trajectory views of an RF quadrupole example in SIMION 8. [35]

the next time step. The time step is continuously adjusted to maximize the trajectory accuracy. A standard fourth-order Runge–Kutta method is used for numerical integration of the ion trajectory in three dimensions.

Concise but exhaustive instructions for the creation of a Workbench in SIMION can be found in Appendix A; an example of a basic geometry file is in Appendix B.

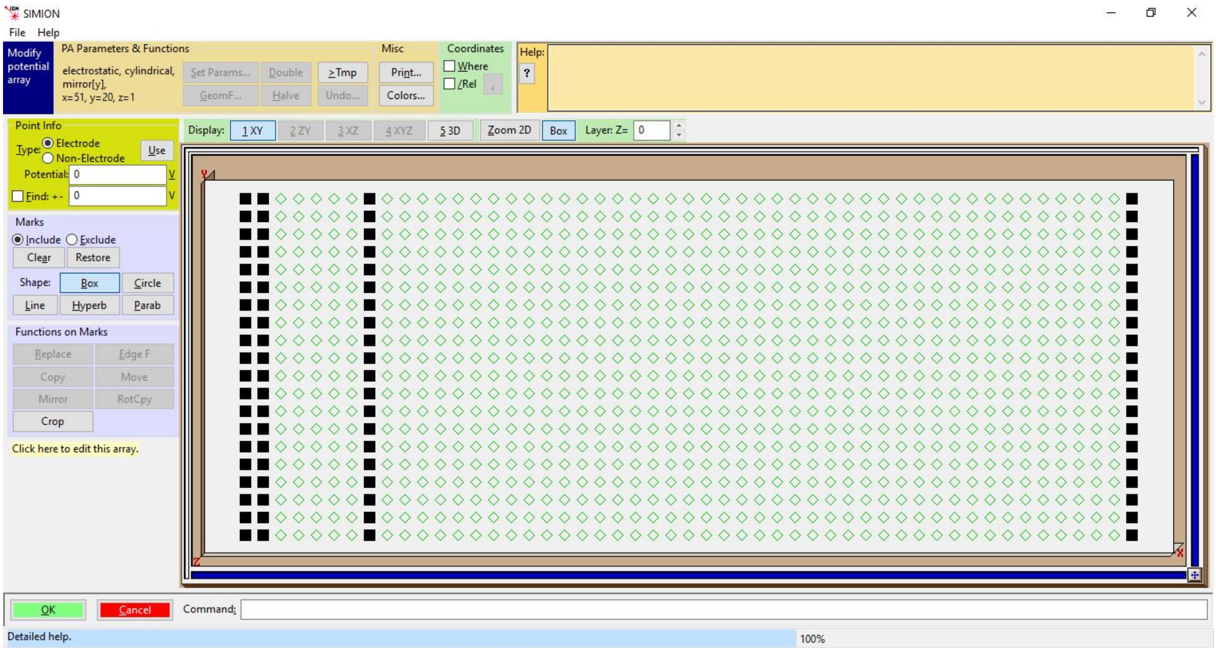

Figure 1.18: Example of Potential Array, as specified in the upper side of the screen this potential array will have a cylindrical symmetry (Fig. 1.19).

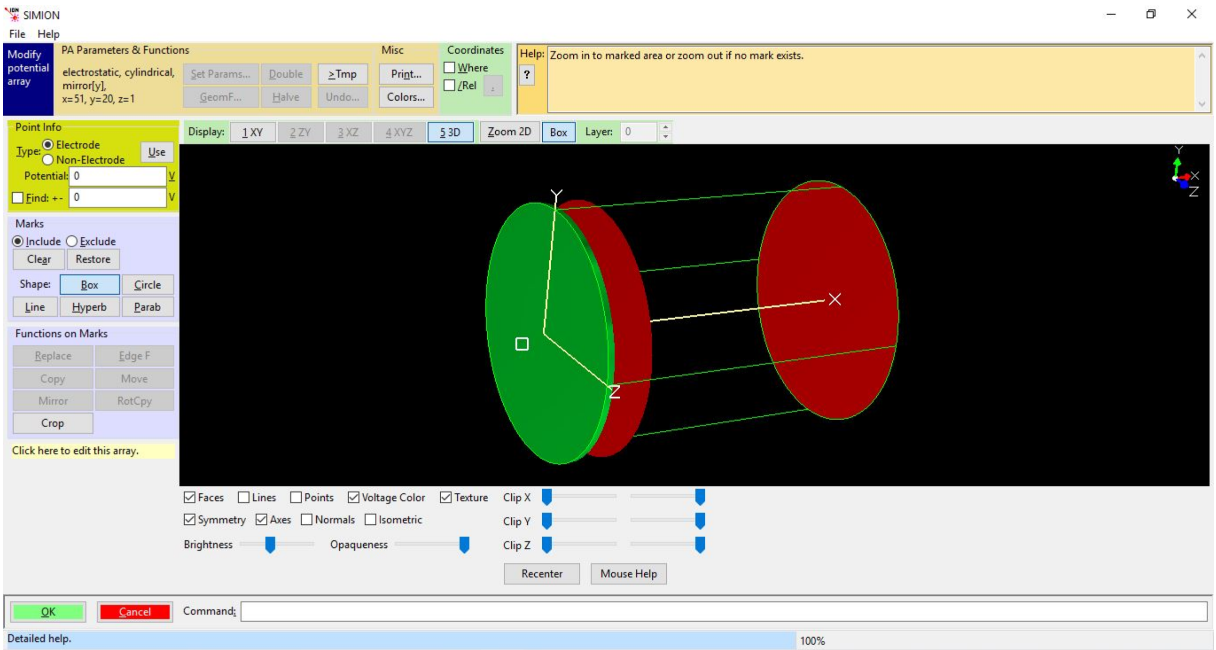

Figure 1.19: Example of the Potential Array in Fig. 1.18 with a 3D view.

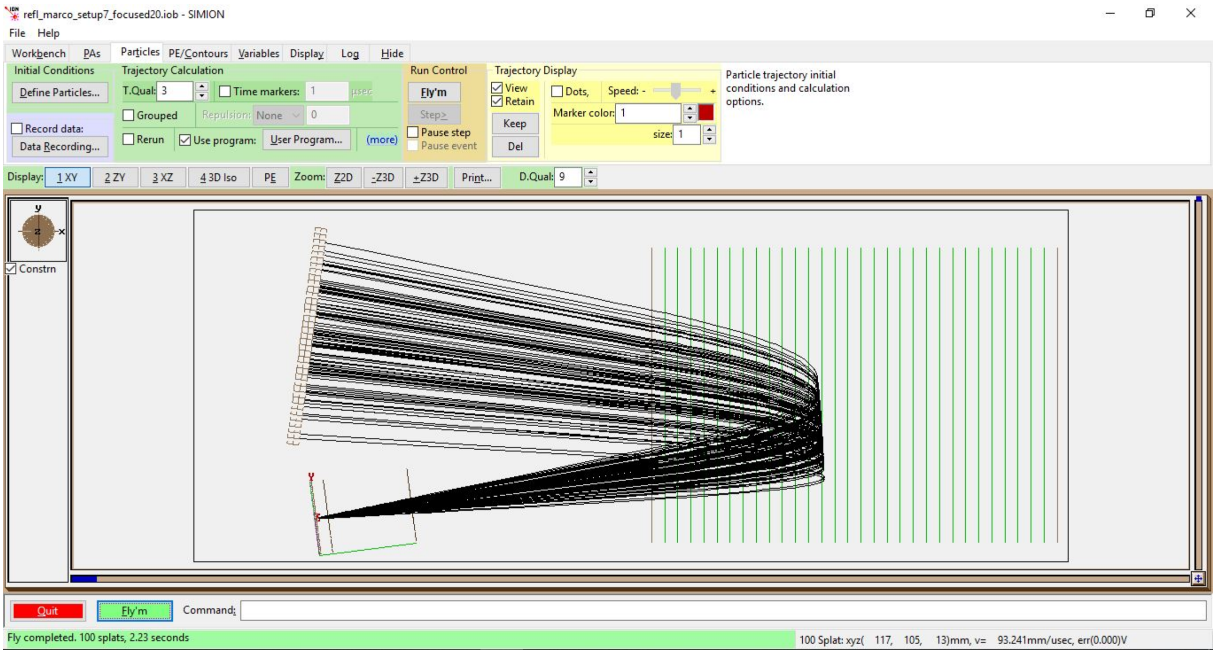

Figure 1.20: Example of Ions Flight in a Reflectron Design.

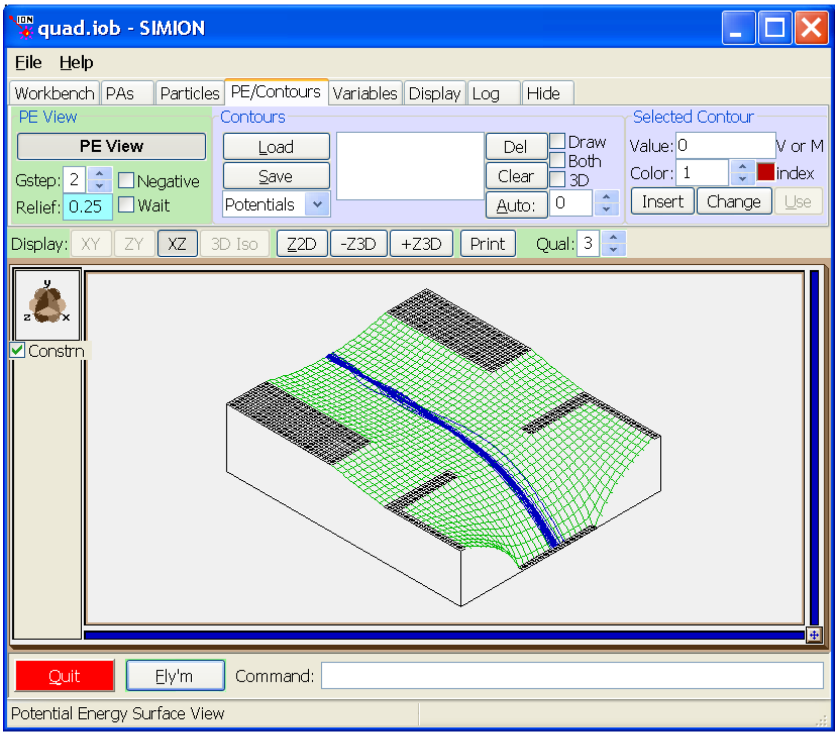

Figure 1.21: Example of potential energy surface. [37]

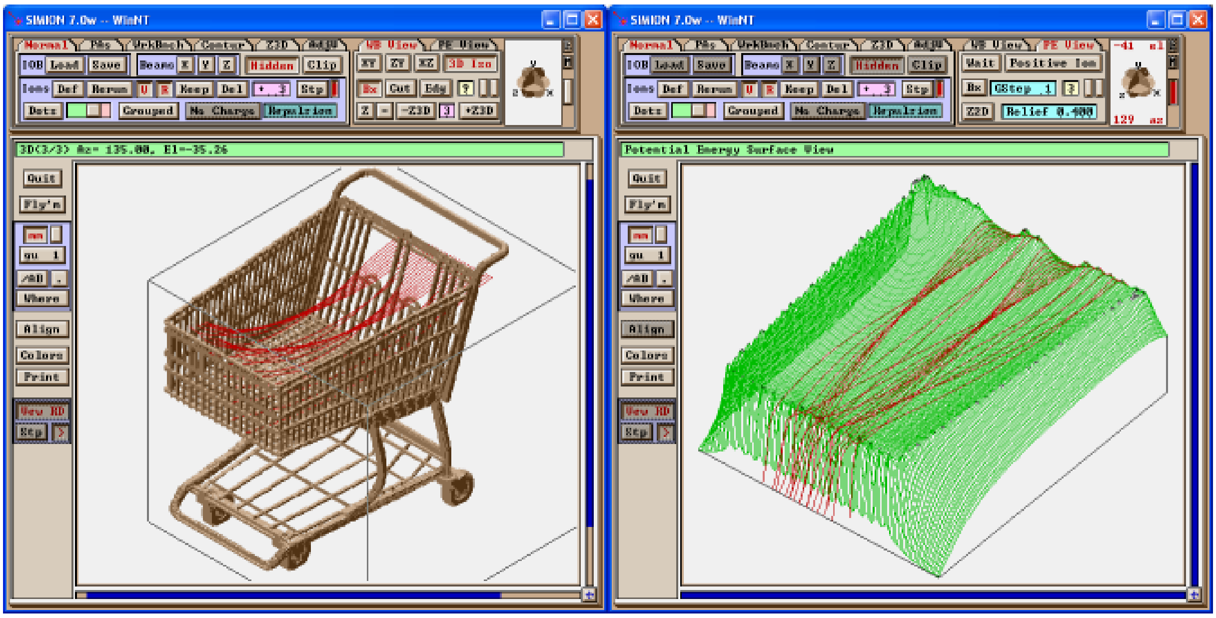

Figure 1.22: (left) Model acting as a non-ideal grid (300 x 350 x 300). Original “shopping cart” STL model, (c) 3D CAD Browser (www.3dcadbrowser.com), by Wenet Locker (2001). 13314 polygons, 13907 points. The shopping cart is held at 120V. Not shown is an enclosing cube held at ground potential. (right) potential energy view of XZ cross section. [38]

Chapter 2

SIMION Simulations

All the simulations were conducted on SIMION, software described in Section 1.5. As already said, this program can simulate trajectories of ions flying in electric or magnetic fields. For this reason, only the flight of the ions between the target and the MCP was inspected, and not the trajectories of particles before the impact.

The simulations were started in the Workbench of the Linear configuration of the TOF Mass Spectrometer. As a first step, a basic sketch of the setup (Fig. 2.1) had to be designed, comprising target, detector and metal grids, all of them with cylindrical symmetry; the total dimensions of the instrument were chosen with the help of a previous analysis on the room availability inside the IRS's laboratory for the construction and location of the vacuum chamber in which the TOF Mass Spectrometer will be placed and tested, so a length of 600 mm and a diameter of 300 mm were chosen. These sizes were used as boundary conditions also for the design of the Reflectron configuration (Chap. 6).

The number, the location and the potential of the metal grids are a matter of optimization, and will be discussed in Chapter 5 while studying the focusing properties of the Linear TOF Mass Spectrometer. For the Linear configuration a single potential array was used, where all the components are coaxial; for the Reflectron configuration instead, three potential arrays were necessary: the source, meaning the target and two acceleration grids, the mirror and the detector (Fig. 2.2).

Once the Workbench is ready, the following step is the particle definition (Fig. 2.3).

The software allows the user to define number, charge, mass and initial conditions (position, velocity and/or kinetic energy, azimuth and elevation) of the particles, either by single values or by sequences and distributions:

- the number of ions is related to the statistical validity of the results and the computational cost of the simulation, so according to the type of simulations, sets of 100, 1000 or 10000 ions were flown;
- the ions were chosen with singular positive charge and with the mass of the 56Fe ions or of the Rhodium ions, the first commonly part of the dust sources for laboratory tests, the second material coming from the target and expelled as ejecta after the impact;
- the origin of the particles was set on the surface of the target, as that is the surface were ions are physically born as a consequence of the impact;
- the problem of the angular distribution will be discussed in Chapter 4, while at first the cylindrical symmetry of the linear system was exploited in order to get rid of one of the two angles: between elevation and azimuth angles, only one of them is needed for 2D considerations. Moreover, since no assumption could be made about the angles yet, a uniform distribution of the elevation angle from $-90°$ and $90°$ with respect to the axis was defined.

The only initial condition left to be defined is the initial kinetic energy, that will be discussed in Chapter 3. The initial energy and angular distributions are of fundamental importance because they are the main reasons for the broadening of lines in mass and TOF spectra: an insight on them is needed to optimize or modify the design of the instrument in order to largely improve the resolution and the general performance.

Every electrode needs to be set to a proper voltage for every test. Even if a standard laboratory on ground can have access to much more electrical power than an instrument on board a spacecraft, the voltages were chosen not to exceed much the capabilities of the instrument on the probe: for this reason voltages not higher than 6 kV were applied in the different tests.

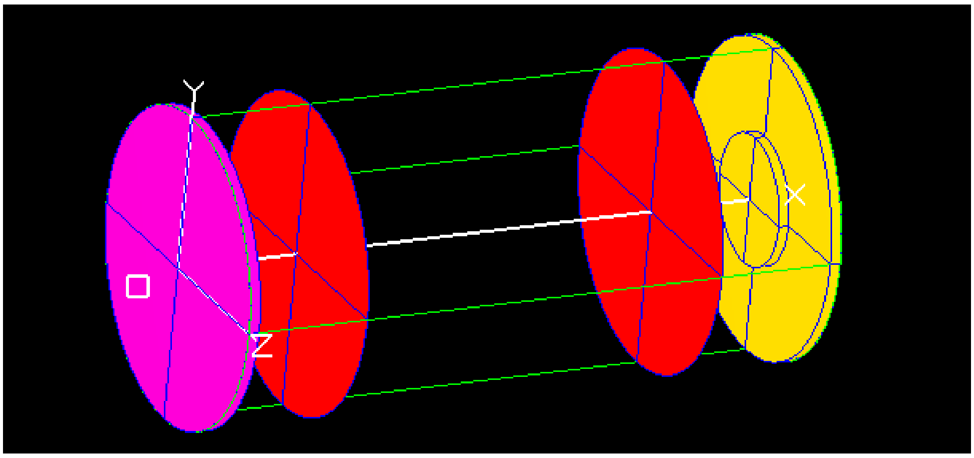

Figure 2.1: Basic Design of the Linear TOF Mass Spectrometer: the purple target, the red grids and the yellow detector are coaxial.

Realistic grids were not included in the simulations because their effect strongly depend on the type of grids used.

Ion-ion Coulomb repulsion was not taken into consideration in these simulations. Two simplifying assumptions were also made in these calculations, that the vacuum was good and so no ion-neutral collisions occurred during the flight [39] and that there were no magnetic field imperfections in the drift region to disturb the ion motion.

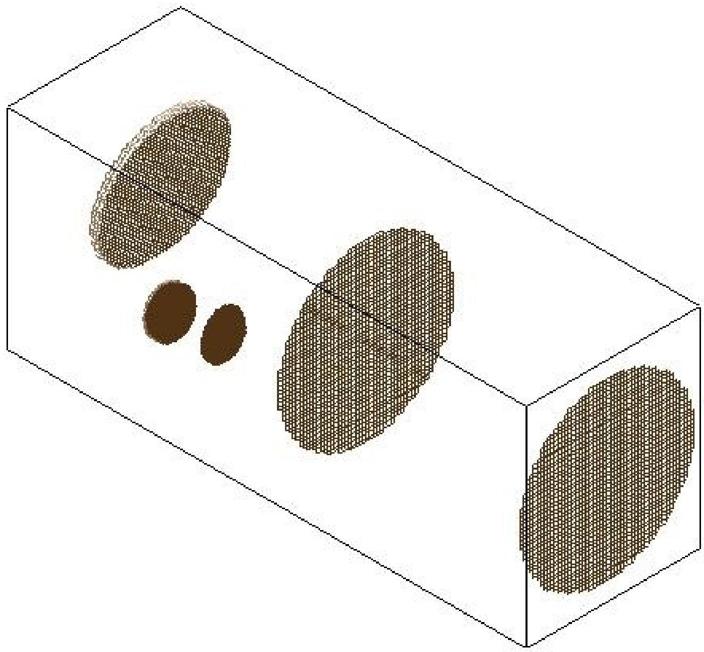

Figure 2.2: Isometric view of the Reflectron setup. The darker circles are the target (on the left) and the acceleration grids (on the right). The single plate on the left is the detector. The other two plates on the right are the grids that represent the entrance and bottom side of the mirror. The casing of the mirror was not included for sake of visibility.

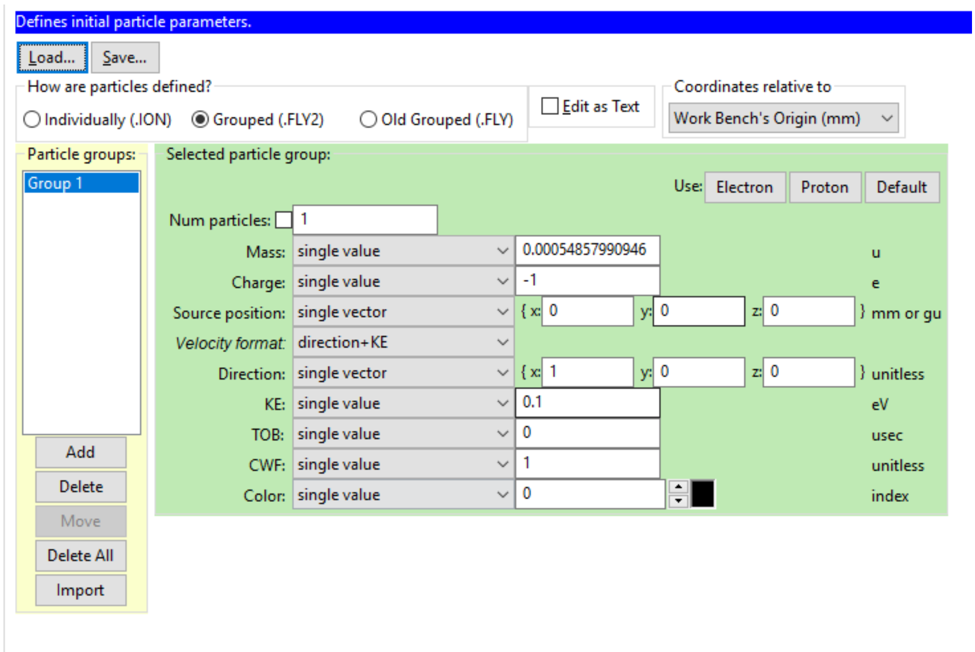

Figure 2.3: Particle definition window of SIMION.

Chapter 3

Energy Distribution

The kinetic energy is a really important parameter because it is related, along with the angular distribution, to the focusing of the particle beam, that is to say the divergence of particles from the centre line: the better the focusing, the more particles are caught by the detector and processed. The study of the focusing parameters will be discussed in Chapter 5. Furthermore, low and almost fixed levels of initial kinetic energy, not always obtainable, can reduce almost completely the broadening of lines in mass and TOF spectra.

In order to work with simulation results as similar as possible to the reality and to prove the validity of the particles definition, an effort was made to find a definition for the energy that was as realistic as possible. A help came from [28], where the mass lines of the spectrogram were inverted for the distribution of initial velocity and subsequently the initial kinetic energies of the ions (Fig. 3.1).

The amplitude of the signal produced by the detector only depends on the number of particles that were detected at the same time; it works almost like a counter. Thus, knowing how many ions had the same initial energy, it's possible to simulate the same distribution out of a fixed set of particles.

This experimental result shows a certain distribution with a peak for low values of initial kinetic energy; a half-normal distribution can be fitted on the real curve and then implemented on SIMION by coding a particle definition in Lua language. A modification of the normal (or Gaussian) distribution was chosen because the contribution of the various factors to the distribution is essentially Gaussian in nature [40]. [21]

At first the parameters of the normal distribution were chosen empirically (Fig. 3.2), trying with various attempts to find the best fit. Later, a Matlab function for fitting distributions (Fig. 3.3) was used on the energy data: the difference in the standard deviation σ between the two fits was negligible, of almost 0.4%.

In many plots in this work the axis may be not scaled and labelled because the picture is just a comparison of curve shapes or because the y-axis is related to the response function of the instrument that is still unknown and not part of this work. This is valid for plots from Fig. 3.2 to 3.6, Fig. 6.3, 6.5 and all the TOF spectra in the Table in Section 6.1.

A further confirmation is given by the Matlab application 'Distribution fitter': this application can generate the chosen distribution type out of a set of data. The energy data is not suitable for this application because it was generated out of a picture, so only the coordinates could be taken but not the actual distribution; the TOF data instead, generated by the energy distribution, could be analysed by the application and a fit was generated (Fig. 3.4). In this case the standard deviation σ differs of 6% by the fit for the energy distribution.

Unfortunately this method has some drawbacks: the accuracy is really low, because no datasheet of the experiment could be retrieved and, for this reason, one had to be created by analysing the picture of the graph as a plot, procedure that leads obviously to errors. In this case, fluctuations in the values of the datasheet are not expected to lead to a big variation of the normal distribution parameters. Then the datasheet was used to produce a particle-by-particle definition to be implemented in the software. The resulting TOFs were then compared as a distribution to the initial kinetic energy (Fig. 3.5).

On the other hand, a high level of accuracy is not requested in this case because the original experimental setup itself cannot be reproduced accurately on SIMION and looking for a precise fit of one particular result of a particular test is of no use. Moreover, the geometry of the setup, the voltages and the conditions of the particles have an influence on the spectrum and then on the shape of the lines of the graph, making it impossible to establish a single value for the parameters of the normal distribution.

As a consequence, the energy distribution should be implemented as a half-normal distribution whose parameters, standard deviation σ and mean value μ, shall be chosen for every test according to the wished features: this was done by writing a Lua code to create the half-normal function (the software interface has only a limited number of distributions in the database, such as the Gauss and the Lorentz distribution, and it cannot accept negative energy values). Such a distribution will be assumed as standard for the rest of this work, except for some modifications of the two parameters, of which the reader will be informed in the case.

The influence on the TOF of the kinetic energy, especially of its range, was studied (Fig. 3.6). The energy, always with the same distribution, was rescaled for different ranges and the results confirmed what already supposed: the variation of the energy is strictly related to the variation of the TOF. Besides, a smaller variation in the time means a sharper shape of the lines in the time spectrum. The mass resolution power R_m of the instrument is by definition

$$R_m = \frac{m}{\Delta m} \tag{3.1}$$

where m is the mass of the ion peak and Δm is the resolving power. This formula can be written in terms of times:

$$R_m = \frac{t_{\mathrm{m,m+1}}}{t_{\mathrm{FWHM}}} m \tag{3.2}$$

where $t_{\mathrm{m,m+1}}$ is the time between the detection of ions of mass m and ions of mass $m + 1$, and t_{FWHM} is the full width of the half maximum [41]. Thus the resolution of the instrument can be calculated from the TOF spectrum. If the mass lines are sharper, that means that t_{FWHM} is reduced and therefore R_m gets higher.

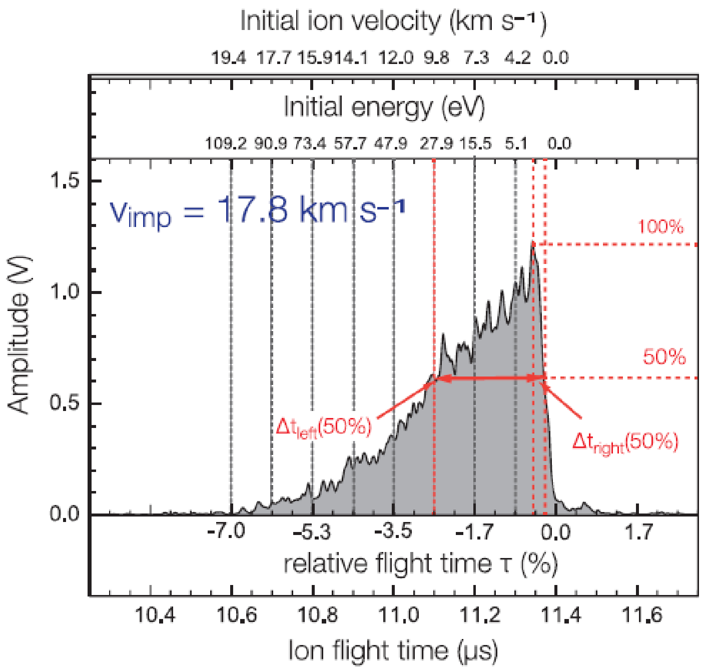

Figure 3.1: The shape of the 56Fe mass line recorded after an impact of an Fe particle on an Ag target at an impact speed of 17.8 km/s. The line profile can be translated into the distribution of initial velocities and energies of the ions. [28]

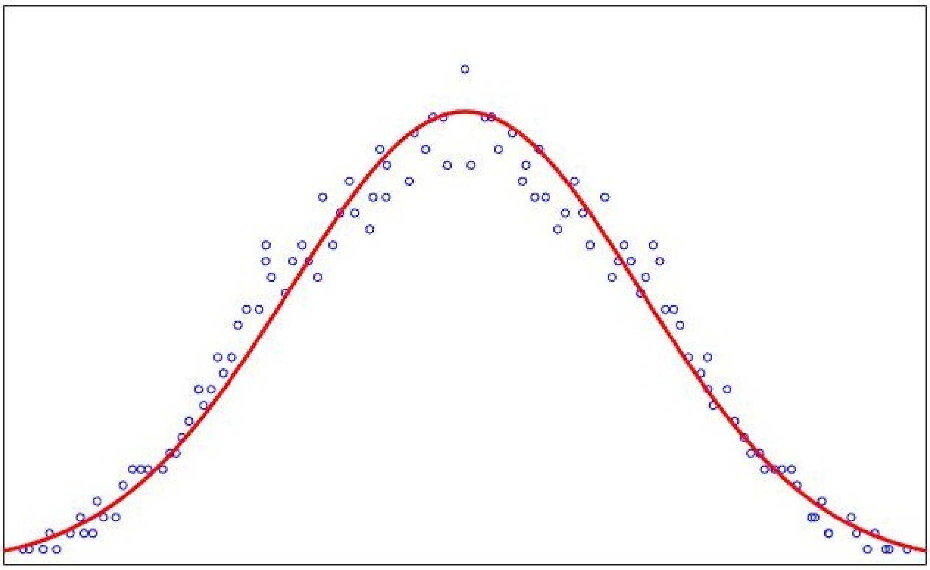

Figure 3.2: Normal Distribution (red) generated empirically and iteratively on the energy distribution extracted from Fig. 3.1 (blue).

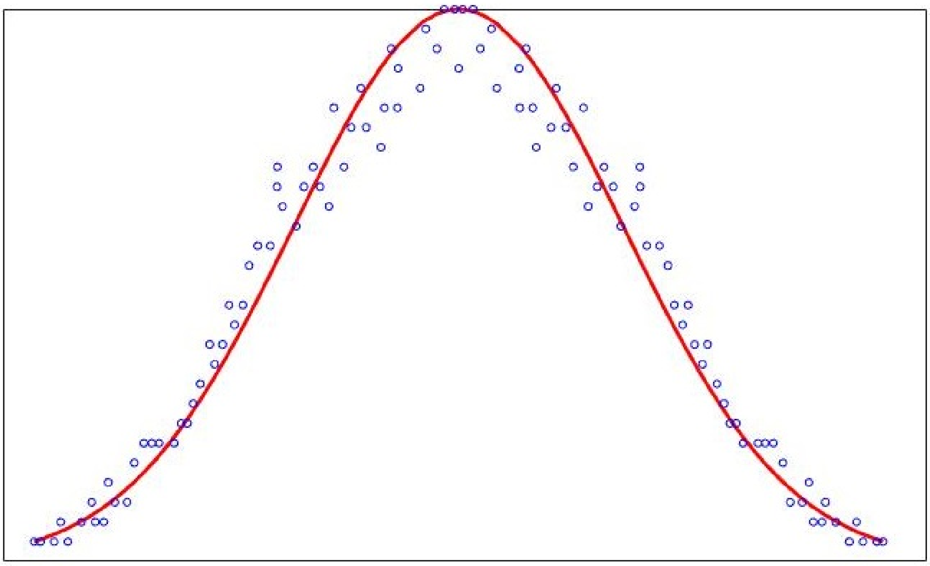

Figure 3.3: Normal Distribution (red) generated by the Matlab function 'fitdist' on the energy distribution extracted from Fig. 3.1 (blue).

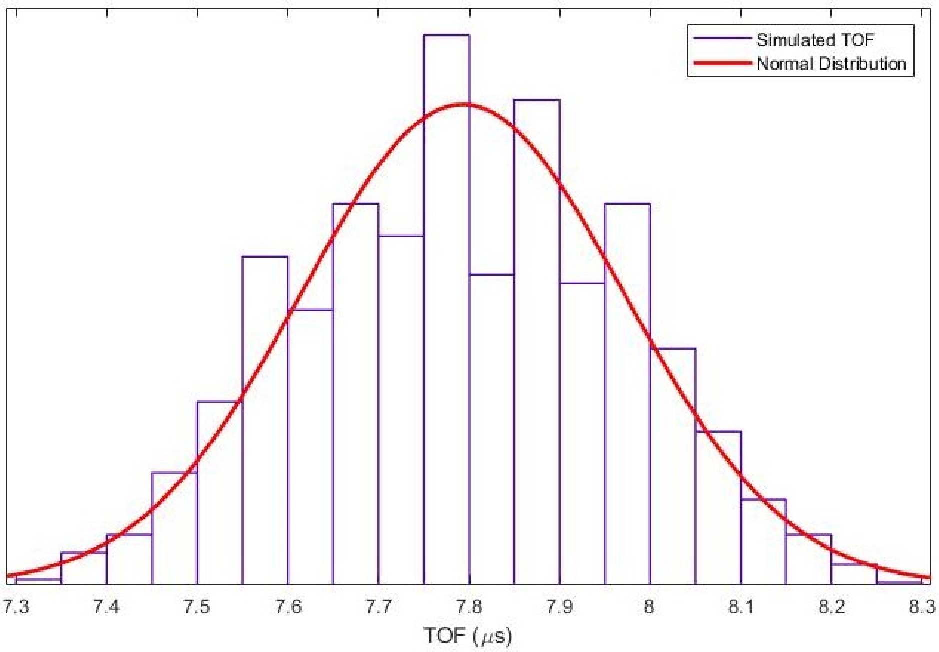

Figure 3.4: Normal Distribution (red) generated by the Matlab application 'Distribution Fitter' on the simulated time distribution.

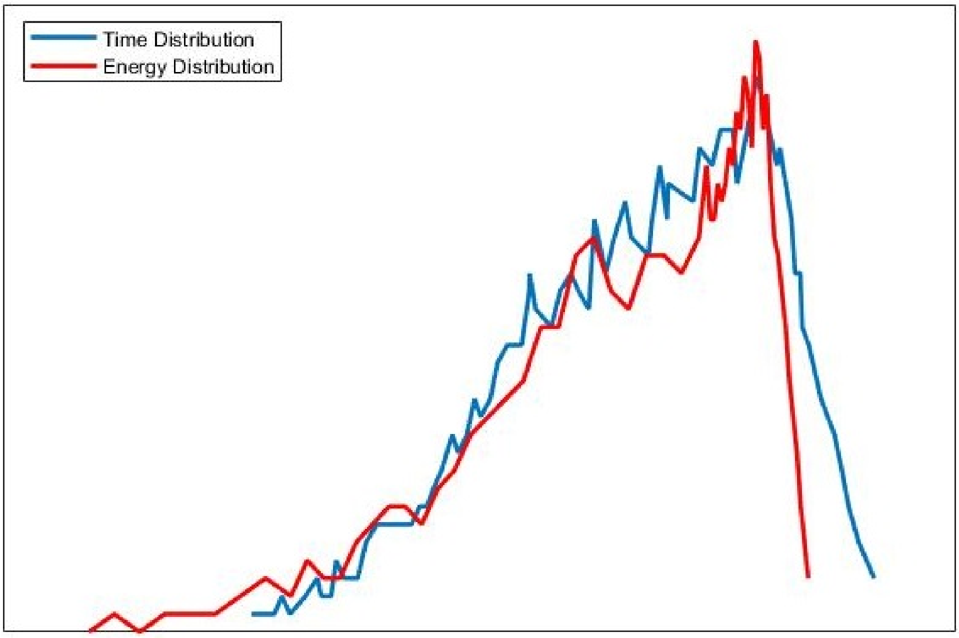

Figure 3.5: Comparison between the initial kinetic energy distribution extracted from Fig. 3.1 and the TOFs computed out of the energies, shifted and scaled.

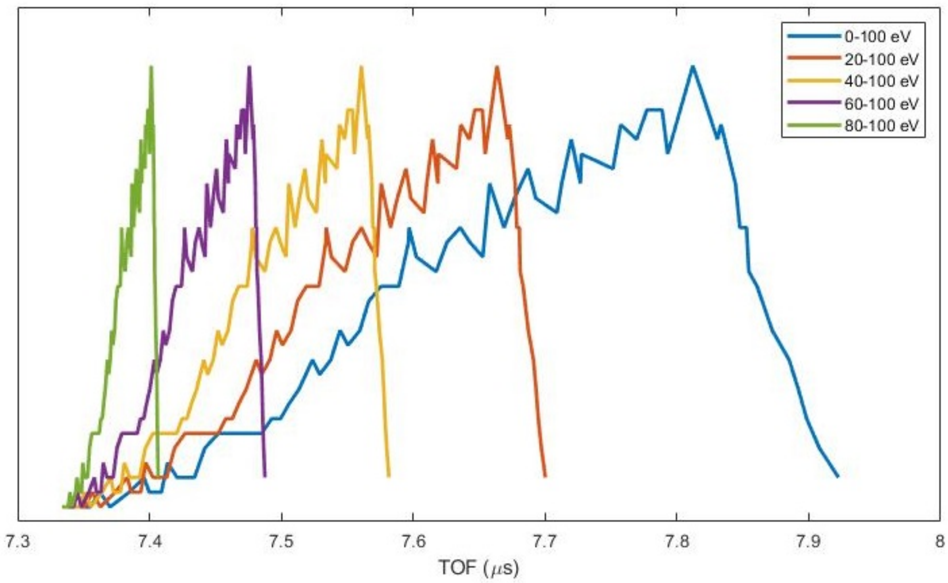

Figure 3.6: Time distribution for different ranges of energy.

Chapter 4

Angular Distribution

Up to now, the angular distribution of ions was assumed uniform since no assumption could be made. The results of studies on this subject, especially regarding hypervelocity impacts, are in fact not yet satisfactory enough to provide an accurate and general definition.

In this work a method for the study of the angular distribution and its dependence on the impact parameters is suggested and simulated. For a better angular resolution, the detector will consist of an MCP with a hole in the middle and a segmented anode (Fig. 4.1): the anode will have a hole too, concentric to the first one and both will have a diameter of 4 mm; through this hole the particles are shot from the accelerator to the target at an angle of 0°.

The anode consists of a PCB board with vapour-deposited gold segments. Each segment will be connected to a separate charge sensitive amplifier: this will generate different signals for each segment, in order to have a more accurate result about the amount and location of the detected ions. The exact dimensions and errors committed in the ring gaps can be found in Appendix C.

To have an overview of the angular distribution at larger angles, several normal MCPs can be placed at the same distance to the assumed impact point at different angles (Fig. 4.2). According to [42], who designed the concept of this configuration, "the inaccuracy of the measurement depends on the diameter of the MCP used; a diameter of 20 mm leads to an uncertainty of about 1,2°". The number and location of detectors is a matter of optimization and compromise between performance and costs: in fact decreasing the number of MCPs lowers the costs but increases the number of needed measurements and so times and costs for the laboratory.

The measurement method will be the same as in the previous tests; the large area and the precise mechanical structure allow the generation of an almost homogeneous accelerating field.

For the simulations, the MCP with the centric hole and the segmented anode is designed (Fig. 4.3) and the results are analysed to predict the behaviour of the accelerated plasma cloud. The anode is segmented in 3 parts, so 4 different work benches are created, one for each segment to be studied separately and the one with the total anode. The particles that hit the MCP are sorted among the 3 different segments, in order to have a better understanding of the angular distribution. The process is then iterated to reduce the errors given by the random generation of the ions, whose parameters follow the distributions previously explained.

The simulations just mentioned were as a first step conducted with a normal angular distribution, that was found the best and most probable assumption: the parameters were chosen to study four different cases, a mean of 0° if the beam is shot through the hole, then of 15°, 30° and 45° depending on the shooting direction (Fig. 4.4). The width of the distribution was assumed and shall be verified by the experimental tests. Please note that the gaps between the segments are a source of loss, but the results of the tests at different angles can fill the lack of data in these spaces.

The average number of detected ions per unit of surface for each segment was plotted along the radius of the anode and fitted with a half-normal distribution for each mean angle of flight. The distribution gets more wide and flat if the mean angle is increased: this is consistent with the ion generation according a normal angular distribution and with the expectations in term of sharpness of the curve.

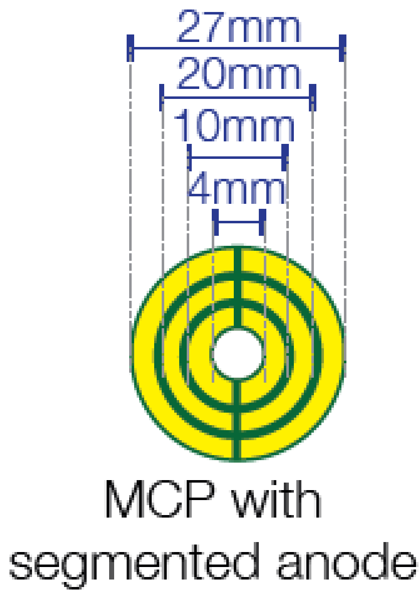

Figure 4.1: Segmented anode. [42]

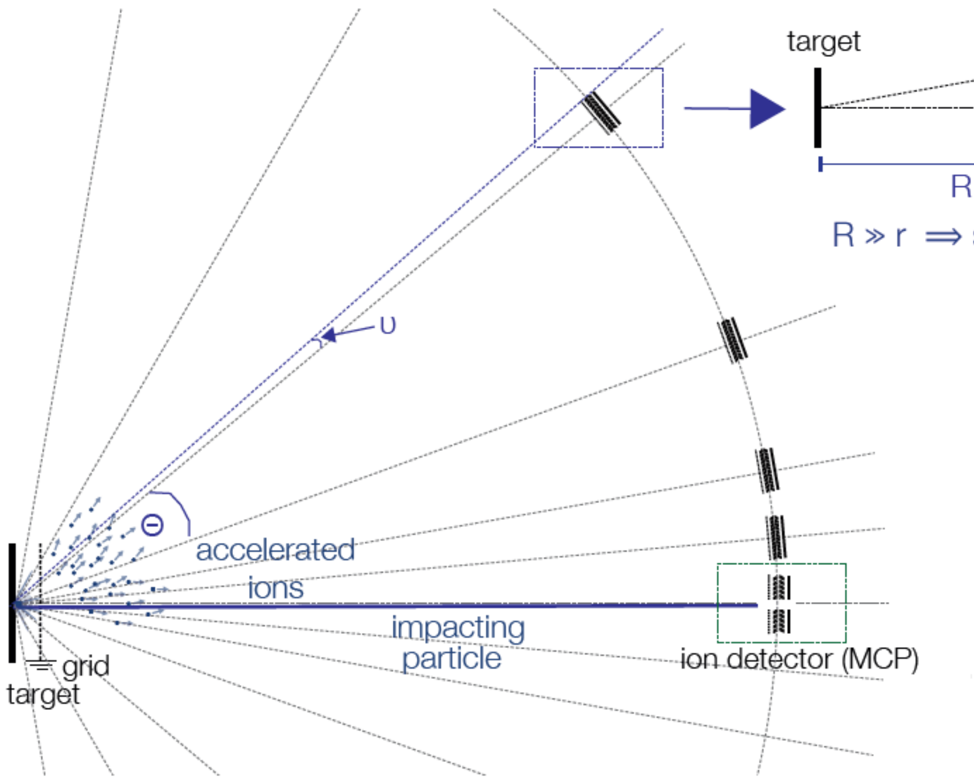

Figure 4.2: Setup for the investigation of the angular distribution. [42]

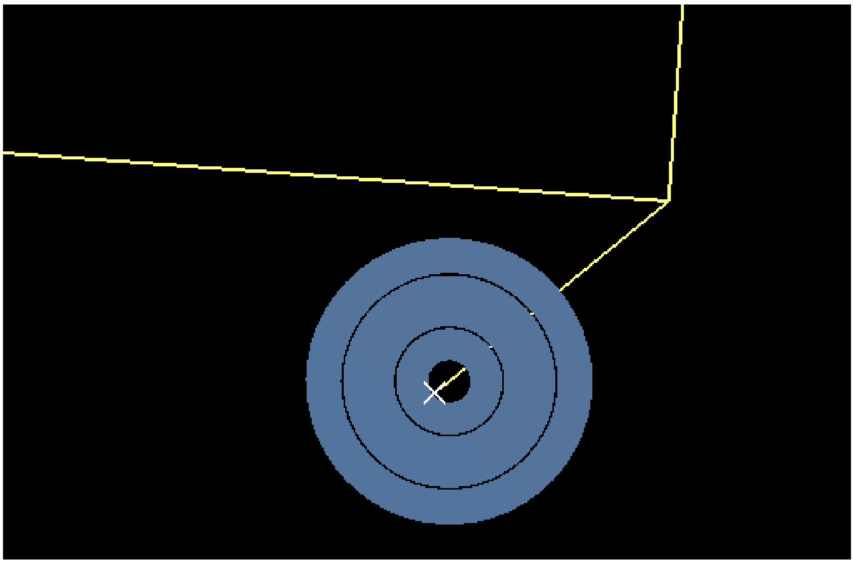

Figure 4.3: Segmented anode designed in Simion.

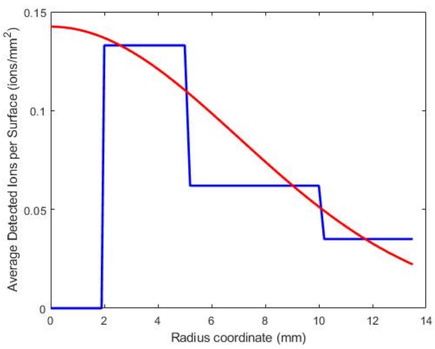

(a) Mean at 0°

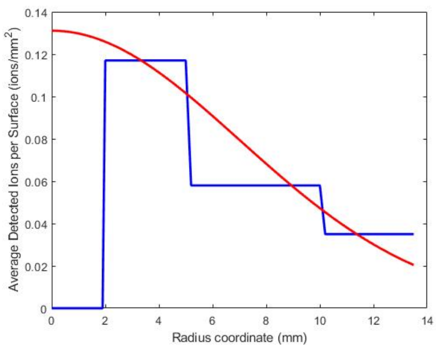

(b) Mean at 15°

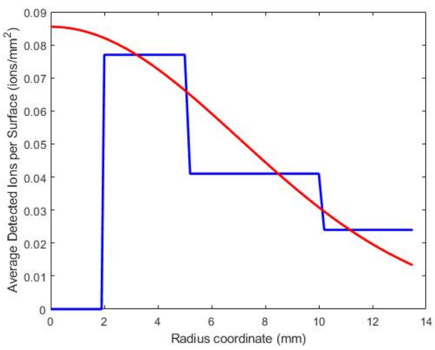

(c) Mean at 30°

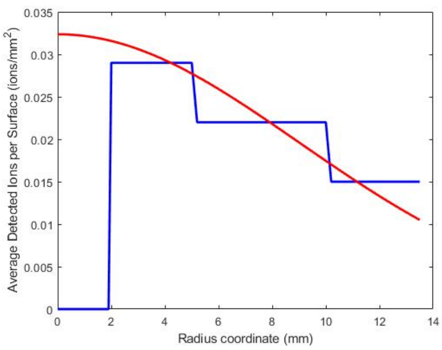

(d) Mean at 45°

Figure 4.4: Average counting of ions detected in each segment per mm^2 with different mean angles depending on the shooting direction.

Chapter 5

Beam Focusing

Here we analyse in a linear configuration the dependence of the beam focusing on the initial conditions of the particles, maintaining the geometry of the setup and the potentials fixed. In particular, we assume to have two metal grounded grids between the target and the detector, so that we find at first an acceleration zone (”zone 1”), then the drift distance (”zone 2”), and then again a second acceleration zone (”zone 3”). Please note that this is the most basic configuration in order to have a drift zone while having target and detector at different and non-zero potentials (Fig. 5.1).

We can write the equations of motion in the two directions x and y

$$\begin{cases} x = v_x t_{\text{tot}} + \frac{1}{2} a_{\text{x1}} (t_1)^2 + v_2 t_2 + \frac{1}{2} a_{\text{x3}} (t_3)^2 \\ y = v_y t_{\text{tot}} \end{cases}$$

where

- v_x, v_y are the initial velocities in the x- and y-directions;
- t_{tot} is the TOF;
- a_1, a_3 are the accelerations in the x-direction in the first and third zones (acceleration zones);
- t_1, t_2, t_3 are the partial TOFs in the first, second and third zones;
- v_2 is the velocity in the second zone (drift zone, the velocity is constant);

Here we see that, with the assumption of an homogeneous electric field whose lines are orthogonal to the centre line, there is no acceleration in the y-direction.

Looking at the second equation, the only one concerning the focusing of the beam, we see that $v_y = v \sin \alpha$ where α is the elevation angle and v is the initial velocity: from Eq. 1.2 this velocity can be written as

$$v = \sqrt{\frac{2KE}{m}} \tag{5.1}$$

where KE is the initial kinetic energy and m is the mass of the ion. For this reason we can write

$$y = \sqrt{\frac{2KE}{m}} t_{\text{tot}} \sin \alpha \tag{5.2}$$

so y depends on $\sqrt{KE}$, $\sin \alpha$ and t_{tot}. Analysing these 3 parameters separately, we see that: the initial elevation angle, as already explained, has no special boundaries except of course the target itself, so it should be considered as a first step uniform and independent; the initial kinetic energy should follow a half-normal distribution as in Chapter 3 and this makes it independent as well; the TOF instead, as we can read in the first equation, is related to the total distance (geometry), to the initial velocity (initial kinetic energy), and to the accelerations (electric field).

This last relation is given us by the equation

$$a = \frac{qE}{m} \tag{5.3}$$

where

- a is the acceleration;
- q is the charge;
- E is the electric field intensity;
- m is the mass;

but $|\vec{E}| = |\nabla V|$ where V is the electric potential, so we can rewrite

$$a = \frac{q\Delta V}{m\Delta x} \tag{5.4}$$

Figure 5.1: Basic Simion Design: the green area on the left is the ”zone 1”, the white one is the ”zone 2” and the green one on the right is the ”zone 3”.

In this way we see that the accelerations are again dependent on the geometry and on the potentials.

As already stated, the complete definition of the geometry is a matter of optimization between focusing and resolution, and will be discussed in the next Section. In any case, the TOF of course isn’t a parameter that can be chosen, but its influence is limited (for our application, it might have variations of around 5% on the average) so it can be ignored in the dependence losing not so much accuracy.

Through simulations, a verification was sought of the previous analysis: sets of particles were flown against a detector of fixed radius and sorted into their final y-position to count which ones were detected and to record their features.

Sorting the ions according to their detection and choosing as a parameter $t_{\text{tot}}\sqrt{KE}\sin\alpha$, we clearly see that, for these particular voltages and geometry, a threshold (Fig. 5.2) of this parameter exists: if the ion is too energetic or its initial elevation angle is too large or it takes too long to reach the end of the path, it won’t be detected.

If the same study is conducted not taking into account the TOF, another threshold (Fig. 5.3) can almost be found, with some fluctuations due to the variability of TOF in μs of about 5% as already mentioned.

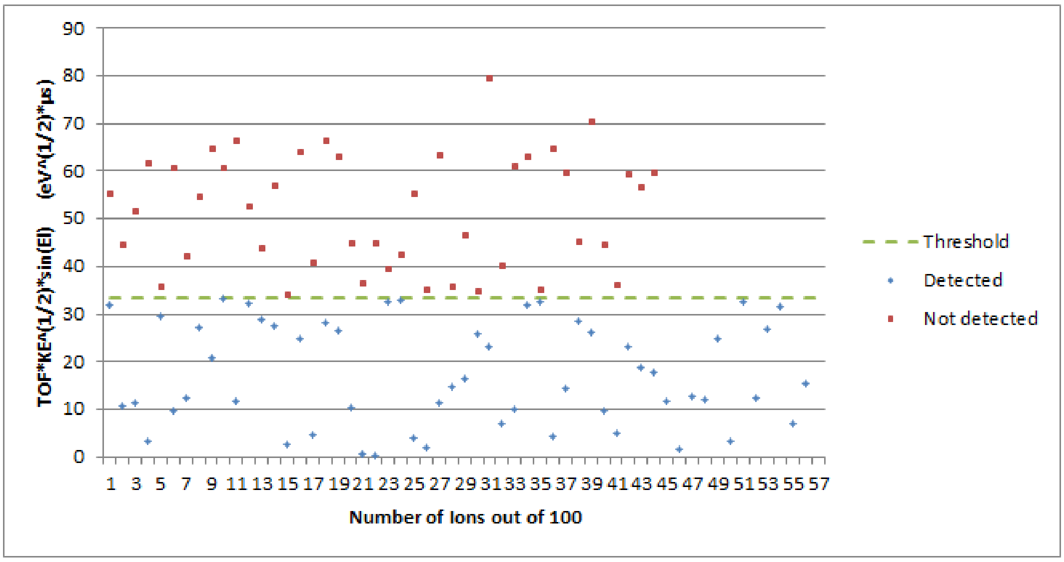

Figure 5.2: Threshold of the parameter $t_{\text{tot}}\sqrt{KE}\sin\alpha$

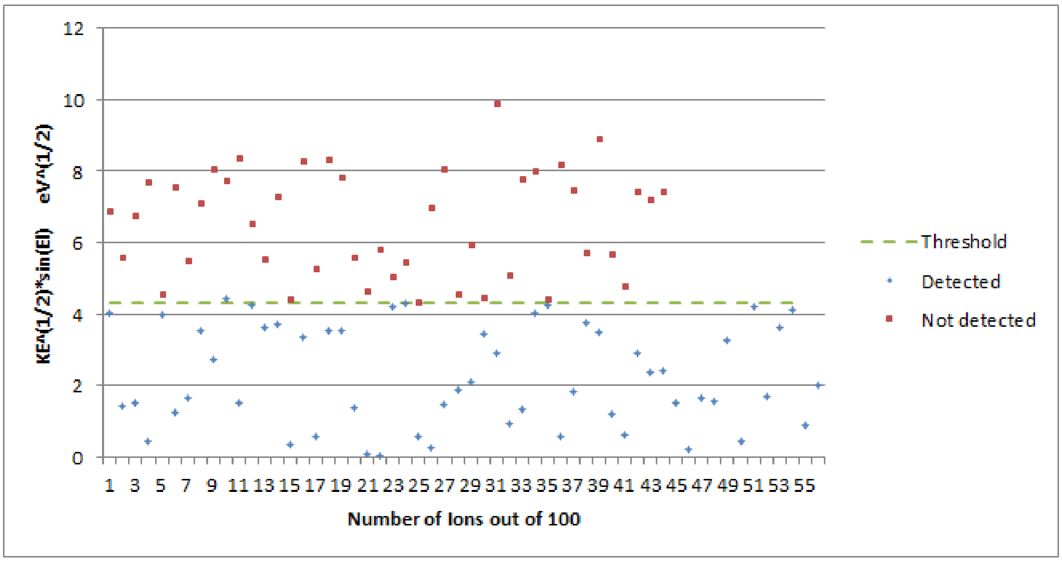

Figure 5.3: Threshold of the parameter $\sqrt{KE}\sin\alpha$

5.1 Beam Focusing Through Potential Gradient

In the previous study the geometry and the voltages, that is to say the gradient of potential, were fixed from the beginning. In this one the effect of the gradient on the focusing will be investigated.

First of all, a consideration is needed: we can choose to have an electric field right after the target or to have a first null-gradient zone, with the free expansion of the plasma cloud, and then an electric field to induce the acceleration. Comparing the two cases, the first of which with a random gradient, it can be easily seen that if the cloud is allowed to freely expand after the impact, many ions are lost in this first zone (Fig. 5.4): this happens because there's still no acceleration along the x-axis, so ions are not pushed towards the detector and they are free to fly in any direction according to their initial angle.

If, instead, the electric field starts accelerating the particles right after the impact, almost all the ions reach the bottom of the instrument, while of course only some of them will be detected (Fig. 5.5). For this reason, the case with an initial free expansion zone should be ruled out of the study.

The best performance caused by the value of the gradient in the first zone was then sought. Two methods were used for a complete overview: single ions with a single value elevation and kinetic energy were flown to prove the analytical calculations and then groups of ions with distributed elevation and energy were flown to see the statistical behaviour. Moreover, the gradients of the two acceleration zones were studied separately. Other two cases were generated by varying only the potentials or only the geometry, since both contribute on the intensity of the gradient.

The first test was made on sets of 1000 particles flown with different potentials in the first acceleration zone; for this analysis, the number of grids was increased from two to four for the sake of flexibility. The simulations were conducted several times and the average values were put into a histogram (Fig. 5.6).

Config. Name	Grad. 1 (V/mm)	Grad. 2 (V/mm)	Grad. 3 (V/mm)	Grad. 4 (V/mm)	Grad. 5 (V/mm)	Rank
3k_linear	33.3	25	25	0	30	
3k_500_0	83.3	12.5	0	0	30	***
3k_2k_500_0	33.3	37.5	12.5	0	30	
3k_2k_1k_500_0	33.3	25	12.5	1.39	30	
3k_2k_0	33.3	50	0	0	30	
3k_1k_500_0	66.6	12.5	12.5	0	30	*
3k_1k_1k_0	66.6	0	25	0	30	
3k_1k_0	66.6	25	0	0	30	**
2k_1k_0	33.3	25	0	0	30	

The table reports the values of the potential gradients of the different configurations, given that the target, the four grids and the detector are fixed at a distance of 10 mm, 40 mm, 80 mm, 120 mm, 480 mm and 580 mm from the origin of the Workbench. The gradients were calculated with

$$(\nabla V)_i = \frac{\Delta V_i}{\Delta x_i}, i = 1 \ldots 5 \tag{5.5}$$

where i is the number the gradient, in this case up to 5 since the target, the four grids and the detector delimit 5 distances; ΔV is the difference of potentials between two elements; Δx is the distance between them. The name of each configuration is explained in the caption of Fig. 5.6. The rank is assigned to the 3 best focusing cases: the best gets three stars (***), the second best two and the third one only one star; this focusing rank was decided only on the total number of detected particles. The worst result belongs to the system where the target is at 2000 V, while in all the other systems the target is set at 3000 V: this means that the higher the potential of the target, the steeper the "slope" (Fig. 5.7) of potential (if the potential of the first grid doesn't change), resulting in a higher acceleration.

Among the other results, the best performances were obtained by the systems that have the steepest gradients at the beginning: in fact, for this particular geometry, the configurations '3k_500_0', '3k_1k_0' and '3k_1k_500_0' were the ones that got a ranking mark. The single-ion test confirmed the results of the statistic study, with a difference of the arrival position in the different configurations in the order of 10^{-4} m. In Fig. 5.6 too the height of the two highest columns is almost the same.

Another confirmation comes from the variation of geometry with fixed potentials: the closer the first grid to the target, that is to say the steeper the gradient, the more the beam is focused (Fig. 5.10). This effect can be really useful as while the grids get closer to the target, the drift distance increases, with a positive effect on the resolution of the instrument.

Regarding the focusing in the second acceleration zone, a consideration has to be made: previously it was shown that the presence of a null gradient after the impact leads to a large loss of particles and to a really bad focusing of the beam. The second electric field, instead, has only the purpose of improving the focusing of ions that were already accelerated so they already have a large component of velocity along the x-axis. For this reason, the effect and the importance of the second electric field is marginal with respect to the first one (Fig. 5.11 and 5.12).

Through simulations based on the variation of the final potential gradient and the comparison of the beam focusing, it was noticed that if the distance between the last grid and the detector decreases, the quality of the focusing decreases too (Fig. 5.13). The explanation is clear: an electric field with the lines orthogonal to the axis of the instrument is not able to accelerate charged particles in the y-direction, it can only increase or decrease the speed of divergence, but divergence is going to happen anyway.

Following this principle, the final grid should be as close as possible to the previous one: the ideal case would be to have a continuous acceleration from the target to the detector, but in this way we would totally erase the drift zone, largely decreasing the resolution of the instrument. A compromise then has to be found evaluating the effects on performances and priorities.

In case the position of the last grid is fixed, a better result can be obtained if the detector is at a really low negative voltage in order to increase the gradient,

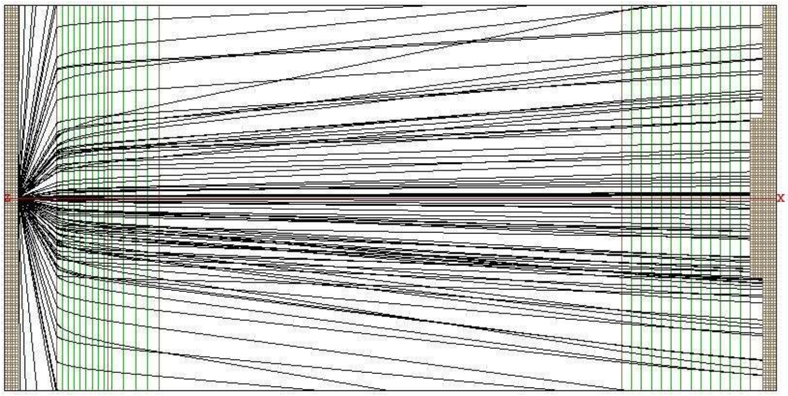

Figure 5.4: Linear configuration with a field-free area in front of the target.

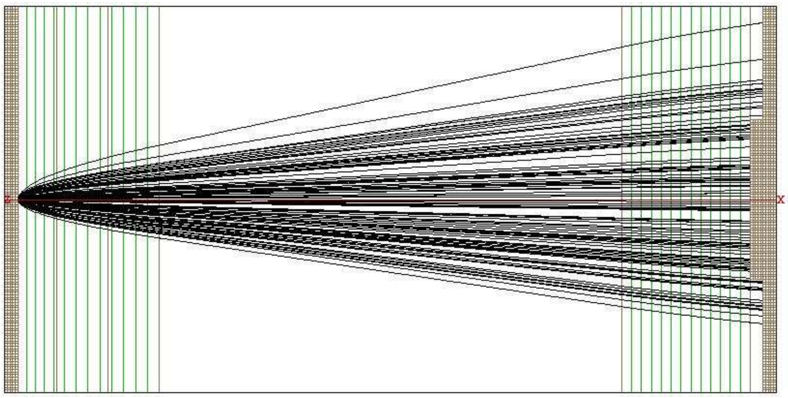

Figure 5.5: Linear configuration in which the electric gradients in both zones are uniform.

but this has to be allowed by the electrical power requirements of the system (Fig. 5.11).

The distances between the grids used in this Chapter are exaggerated compared to a realistic case of a laboratory model (the first grid can be just a few mm far from the target). Nonetheless all the considerations remain valid if the gradients are properly re-scaled.

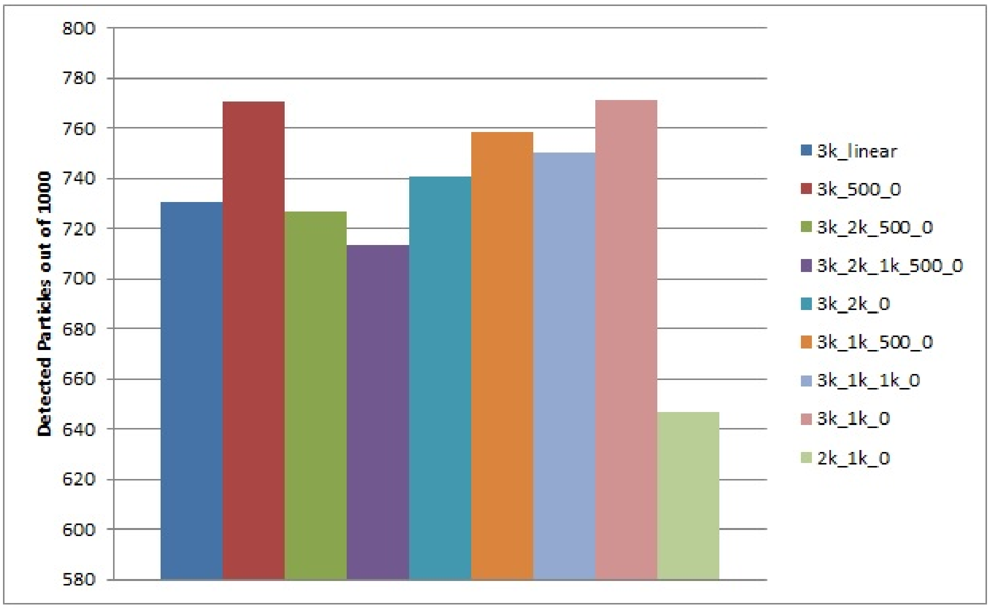

Figure 5.6: Detected Particles for Potential Gradient: each column stands for a different set of potential gradients through the "zone 1": the first number means the potential of the target, the second means the potential of the first grid, the third the potential of the second grid and so on until the fourth grid. After the first '0' in the name of the column, it means that the following grids are at 0 V. The detector is fixed at -3000 V. '3k_linear' means that the target is at 3000 V and the following voltages are decreasing linearly.

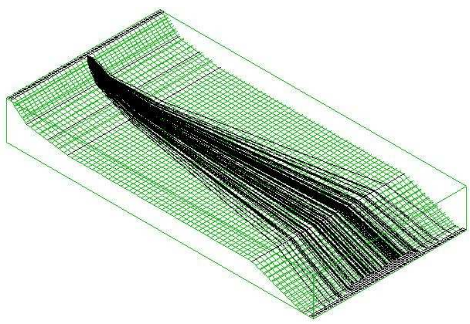

Figure 5.7: Potential Slope

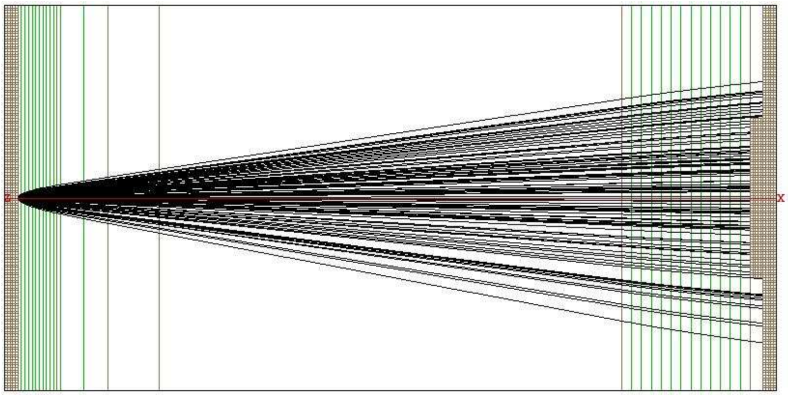

Figure 5.8: Linear configuration with a high potential gradient between the target and the first grid.

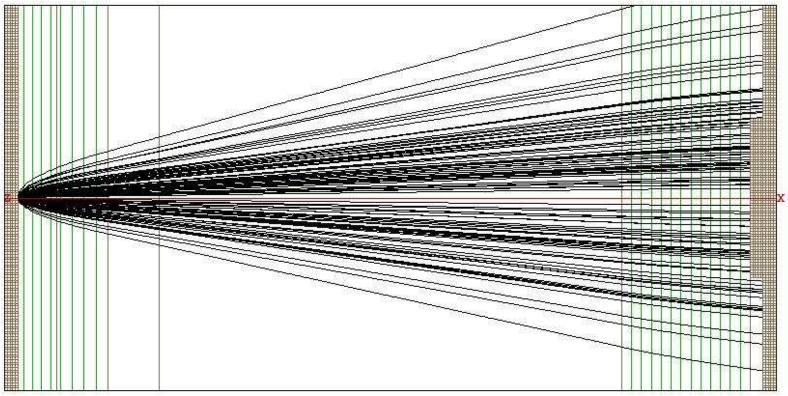

Figure 5.9: Linear configuration with a low potential gradient between the target and the grids in "zone 1".

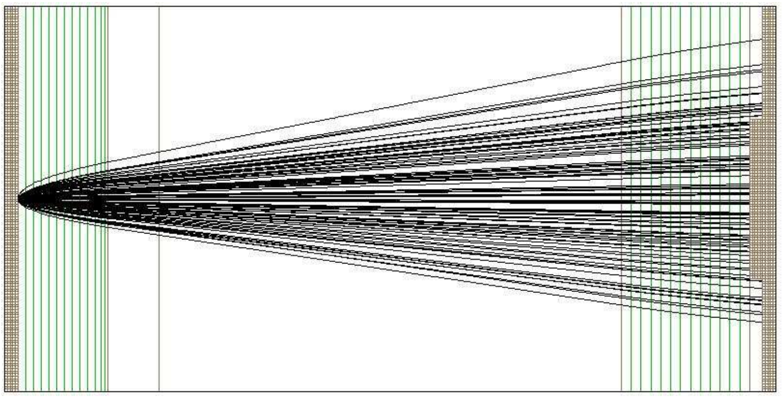

Figure 5.10: Linear configuration with the first grid placed far from the target.

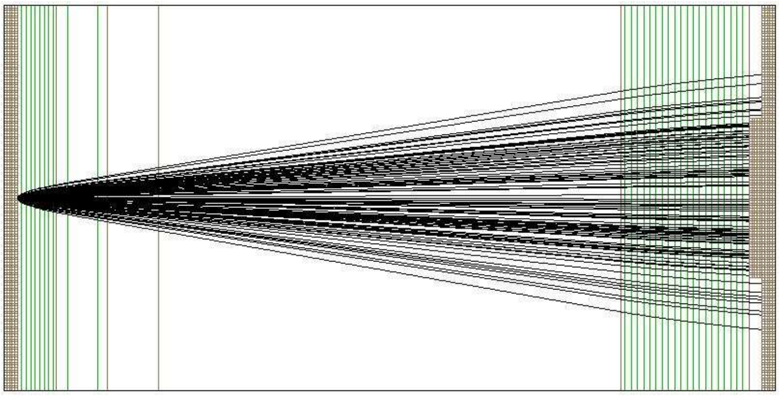

Figure 5.11: Linear configuration with the detector set to -6000 V.

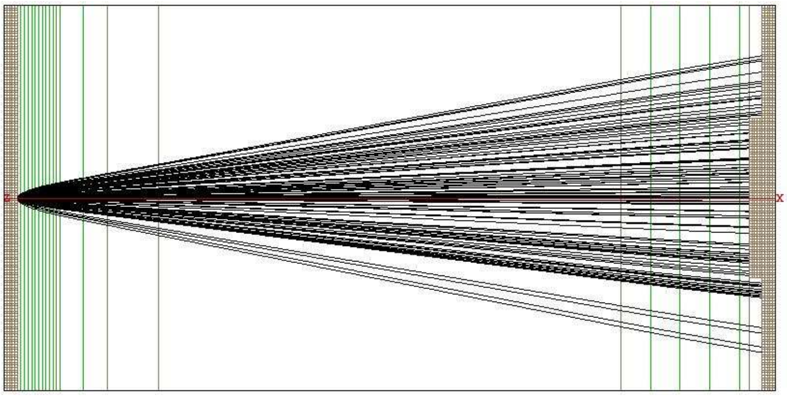

Figure 5.12: Linear configuration with the detector set to -1000 V.

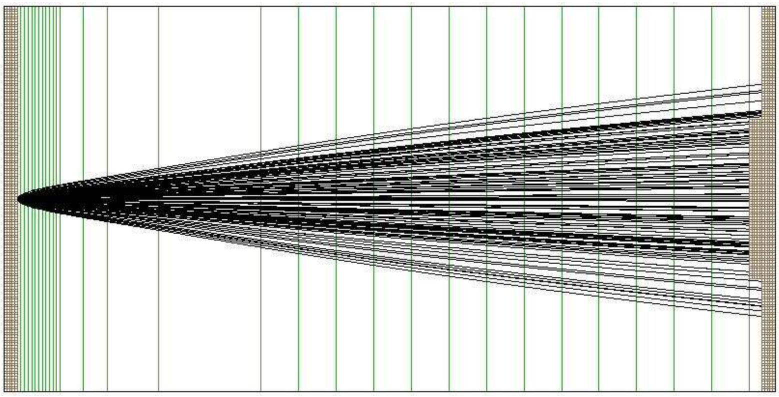

Figure 5.13: Linear configuration with the last grid placed far from the detector.

Chapter 6

Reflectron

The Reflectron is a type of Mass Spectrometer that, through proper trajectory angles and a reflecting electric field, can achieve better mass resolutions than the Linear Mass Spectrometer. The concept is partly the same, at least in the first part: the ions in fact are generated by an hypervelocity impact of dust on a target, then plasma is generated and an electric field accelerates the positive ions in a certain direction.

A Reflectron doesn't actually make a correction of the initial spatial, temporal or velocity distributions and, in fact, the temporal, spatial and velocity distributions at the target focal plane are transferred to the detector focal plane formed after reflection with some distortion. [43]

In the Reflectron configuration, ions are not directly accelerated against the detector: they are in fact pushed into an electric mirror, that is to say a hollow cylinder with a negative electric field. Both the accelerating fields of the target and the mirror are assumed linear and homogeneous. The ions are decelerated inside the mirror until their velocity gets null and then they are accelerated in the opposite direction. Defining the mirror reference system as 'xyz', the ions flying through it maintain the same velocity orthogonal to the mirror's axis, v_y, while the one parallel to it keep the same intensity but gets an opposite direction, that is why it is called "mirror"(Fig. 6.1). Due to these features, two ions of equal mass but different kinetic energies will get to the detector at the same time, since the more energetic ion will fly deeper into the mirror. For this to happen, two conditions are required: first, the Reflectron needs to be focused, this means that the potentials and the position of target, mirror and detector should be chosen such that the drift time is equal to the mirror time [44]; second, the energy variation shouldn't be too high, typically less than a few percent [45]. If the energies in fact are too different, the differences in the TOF spectra are not negligible at all (Fig. 6.3).

This second condition has an effect on the first one too: in fact the instrument can be focused only for a certain level of initial kinetic energy so if its range is too big, the performance drops.

The two conditions, especially the second, are hard to obtain if particles are ionized by an impact, as in our case: as already stated, if the ionization is generated by laser pulses, as in most chemistry laboratories, the initial angle and kinetic energy can be of course better controlled than with an impact ionization. For this reasons, a high resolution for this instrument coupled with the impact ionization is not to be expected.

A parabolic mirror [46] can perform infinite order focusing, i.e. the ion TOF does not depend on the initial kinetic energy of ions at all; such mirrors are also referred to as ideal reflectrons. A potential drawback is that it doesn't have a field-free region which is generally required in TOFMS for mounting detectors, lenses, energy filters, etc. [41]

A setup for the Reflectron was designed and focused for an initial kinetic energy of 20 eV, that could be a likely average value for our conditions. The source, containing target and acceleration grids, and the mirror have realistic sizes; the detector instead has a much bigger diameter than a normal one in order to obtain information on as many ions as possible (Fig. 6.1). The reliability of the setup was proved comparing the shape of an experimental TOF Spectrum produced by an *in situ* dust measurement (Fig. 6.4) and a spectrum generated with this workbench (Fig. 6.5).

6.1 Spatial Distribution

The impacts of 10000 ions on the detectors were recorded and analysed in order to see their spatial distribution.

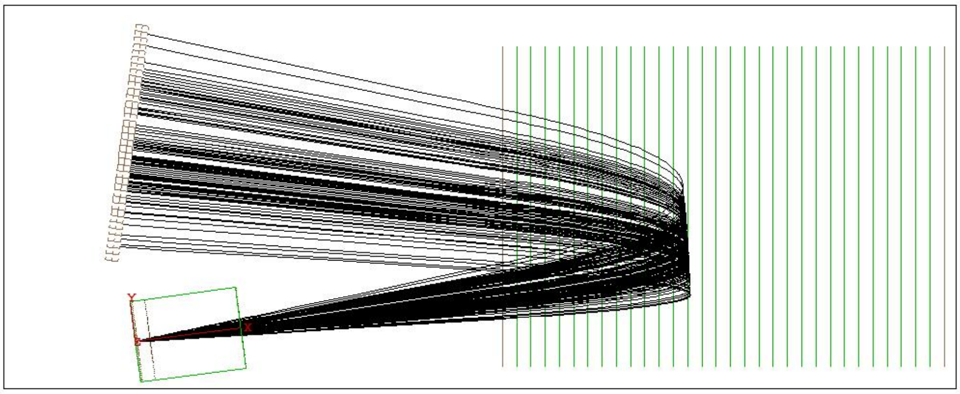

Figure 6.1: Example of ions trajectories in a Reflectron.

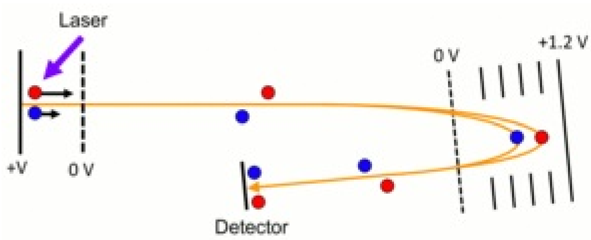

Figure 6.2: Reflectron ion mirror schematic. Two ions with the same mass and charge but one with higher energy (red) are accelerated into a field-free drift region. The ions are reflected by an electrostatic potential in the ion mirror. The higher energy ion takes a longer path through the reflection and is behind the lower energy ion (blue) at the exit. The detector is placed at the point where the higher energy ion overtakes the lower energy ion for energy focusing. [45]

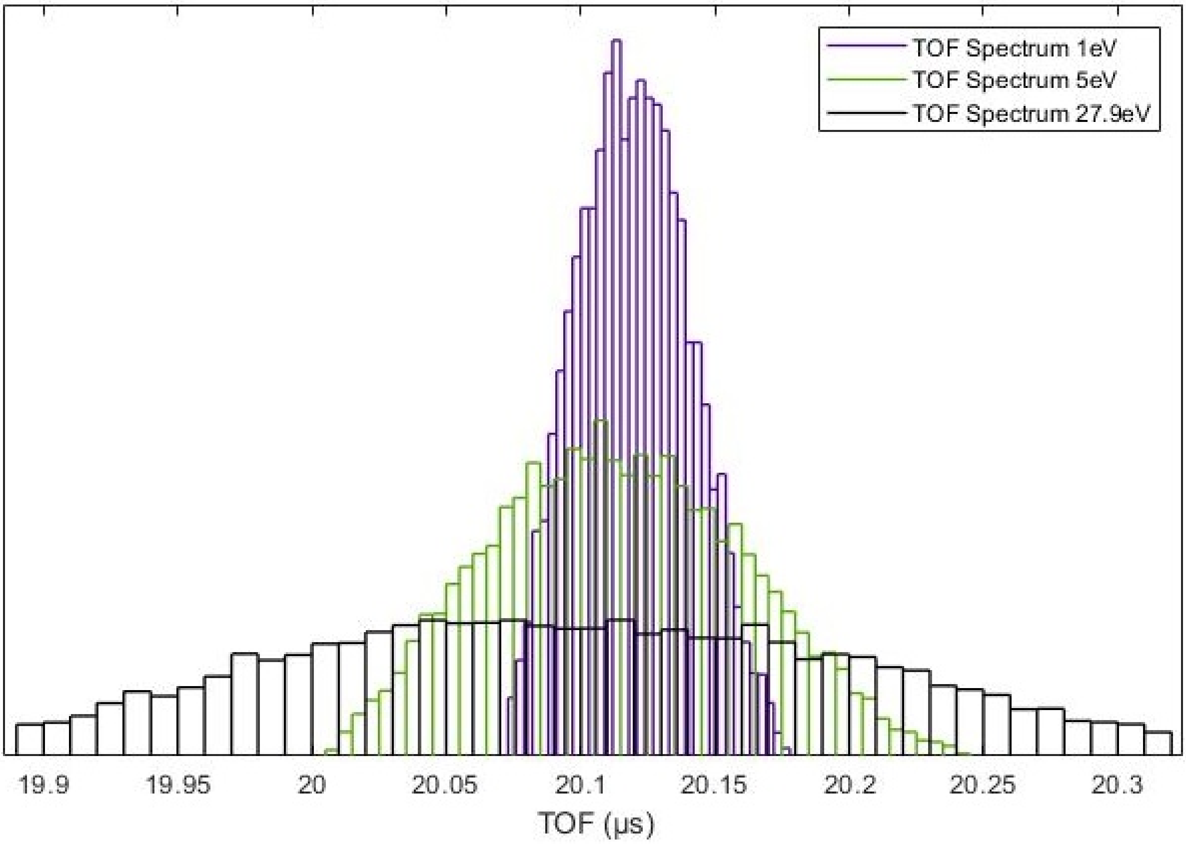

Figure 6.3: Comparison of TOFs of the same sets of particles at 1, 5 and 27.9 eV

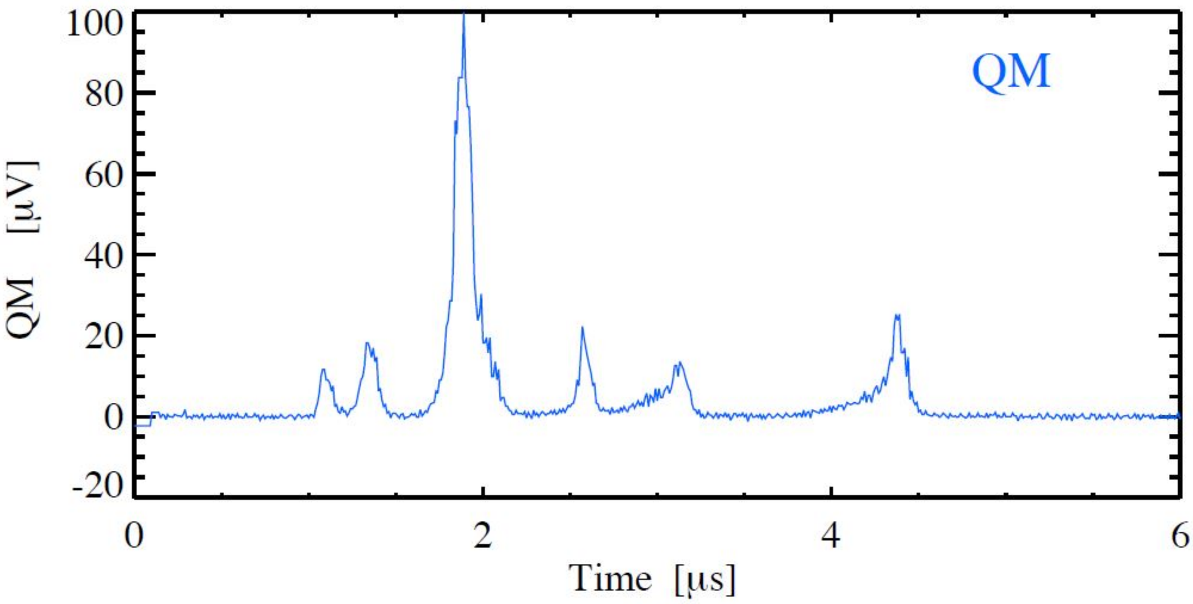

Figure 6.4: TOF Spectrum of an interstellar dust particle with an impact velocity of about 30 km/s. Data by CDA-Cassini, Impact occurred 2009-113T15:57

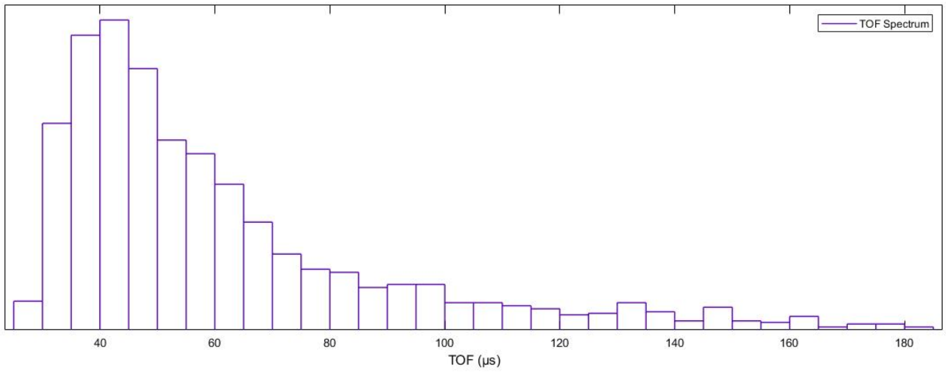

Figure 6.5: Mass Spectrum of Rhodium ions in the designed Reflectron configuration.

A study was conducted through simulations of iron ions (56Fe), with mass of 55.9345 amu, with angular and energy distributions in different combinations. For the angles, cosine, uniform and normal distributions were used; for the initial kinetic energy fixed values of 1 and 20 eV and the half-normal distribution explained in Chapter 3 was used, along with its variation with the standard deviation σ divided by 2. The arrival coordinates, the TOF spectrum and the FWHM (Full Width at Half Maximum) were recorded and compared.

Angular and energy distribution	**Detector Print**	**TOF Spectrum**	**Peak (μs), FWHM**
Cosine, 1 eV	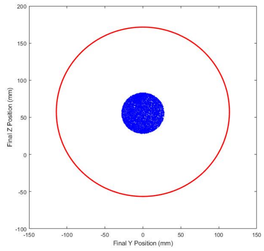	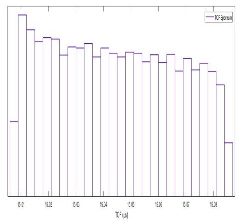	Around 15.01, 0.075
Normal, 1 eV	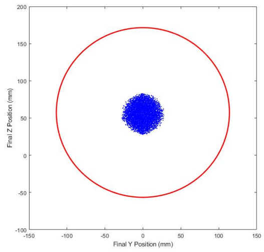	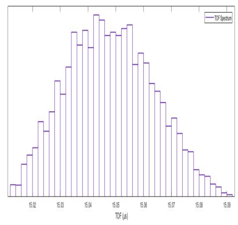	15.043, 0.04
Uniform, 1 eV	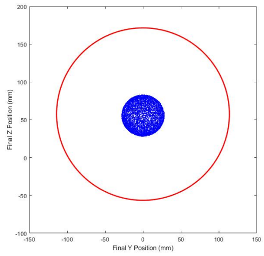	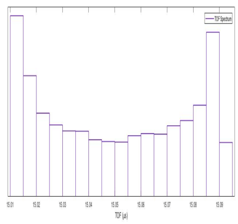	15.01/15.09, 0.08
Cosine, 20 eV	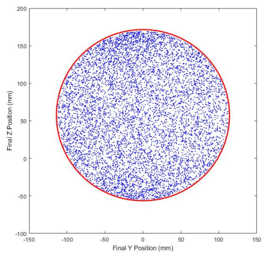	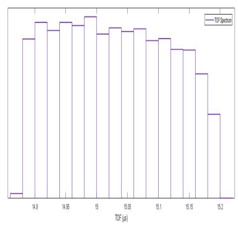	Around 15, 0.3
Normal, 20 eV	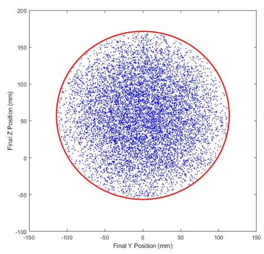	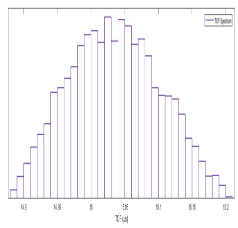	15.025, 0.19

Uniform, 20 eV	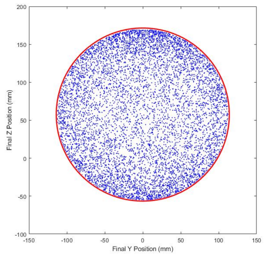	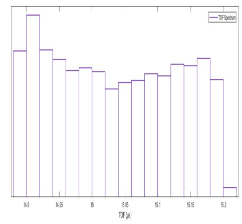	Around 14.9, 0.32
Cosine, Half-normal	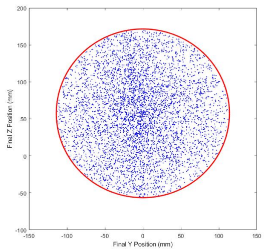	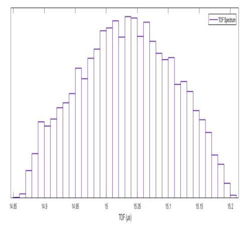	15.035, 0.22
Normal, Half-normal	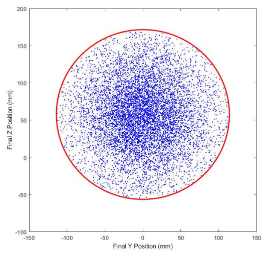	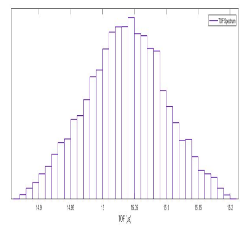	15.045, 0.14
Uniform, Half-normal	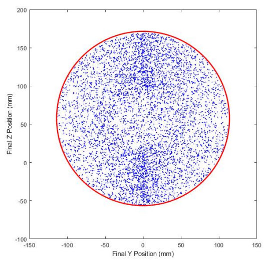	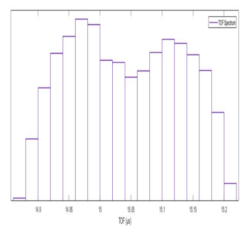	14.97/15.15, 0.28
Cosine, Half-normal with $\frac{\sigma}{2}$, μ=0	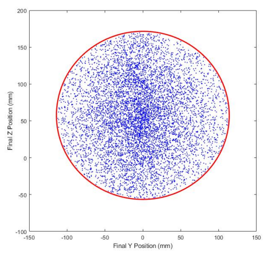	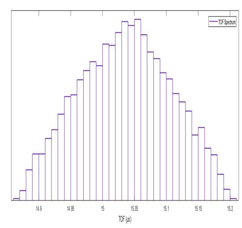	15.05, 0.19
Normal, Half-normal with $\frac{\sigma}{2}$, μ=0	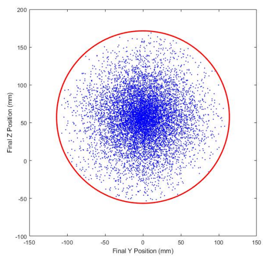	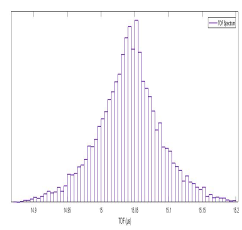	15.05, 0.065

Uniform, Half-normal with $\frac{\sigma}{2}$, μ=0	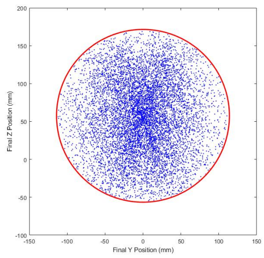	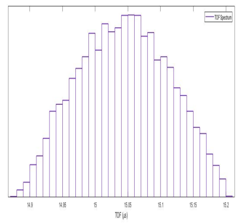	Around 15.04, 0.23

As it may be seen, both angular and energy distributions have an effect on the shape of the TOF spectrum, but if the energy is fixed (or its range of variation is little enough), the shape of the spectrum resembles almost totally the one of the angular distribution, so in this case the spectrum can be used directly to study the angular distribution after the impact; again let me repeat that this condition of fixed energy is hardly likely due to the nature of the ionization, that is to say because of a hypervelocity impact. Another feature that has to be noticed is that the best performance between the ones here studied is obtained if the angular distribution is normal and of course it gets even better for low values of standard deviation σ.

In pictures 'Uniform, 20 eV' and 'Uniform, Half-normal' we notice a zone right in the middle where the ions seem to be less dense: this is caused by the fact that the energy distribution has a peak for values slightly greater than 0, so the half-normal distribution has a mean value μ at 0.00952 eV; if the distribution is shifted to a mean value equal to 0 eV, the less dense zone disappears (as in the last three rows).

6.1.1 Uniform Distribution

A special case has to be mentioned separately: the uniform distribution. This was in fact one of the possible distributions, even if the less likely, that was simulated and compared with the others. Unlike the others, this distribution caused some problems, especially when the software had to combine two identical uniform distributions on the elevation and azimuth angle.

At the beginning, in the particle print on the detector, it was noticed that there was an area in the middle, like a vertical line, in which the particles seemed to be more densely distributed (Fig. 6.6). In order to understand the reasons of this, other tests were conducted including one with the linear TOF mass spectrometer in its most basic setup with no potentials: the ions, with fixed energy and a uniform distribution of both angles from $-90°$ and $90°$ had to fly in a straight line from the target to the detector with no obstacles nor accelerations. The result, looking from the plane of the detector, was the same: more particles were created in the y direction than in the z direction, despite having the same distribution for both directions (Fig. 6.7).

Since particles with really large angles are less likely to be detected, a uniform distribution for both angles from $-70°$ to $70°$ was tested with better results: the "vertical line" seems to disappear in the print (Fig. 6.8). Performing some more tests, another problem with the last distribution occurred: if the distribution has a smaller range, the print is not circular any more, but the upper and lower side of the circle get cut; the smaller the range, the more the circle is cut and thin (Fig. 6.9 and 6.10).

Analysing the print not after the mirroring but right after the first acceleration zone, that cannot change the shape of the spatial distribution, it became clear that the ions were created with that particular pattern, not consistent with the physics of the system (Fig. 6.11). In the end, a distribution from $-5°$ to $5°$ generated a print with the shape of a square (Fig. 6.12).

A further confirmation of this was obtained by looking at the source from an isometric point of view. The first grid in front of the target was made solid and impenetrable to be used as a detector (Fig. 6.13). From that particular point of view, only the ions with greatest angles were expected to be seen, and this is indeed what happened. But while a uniform angular distribution was commanded and expected as well, performing several runs with a range from $-70°$ to $70°$, all of them with almost the same pattern, it was obvious that the particles were generated not uniformly, as it is seen in Fig. 6.14.

Graphic effects, projection effects or fluctuations should not be considered as possible causes for this, since the same simulations were run many times and analysed from all points of view; moreover, sets of 1000 or 10000 ions were flown each time.

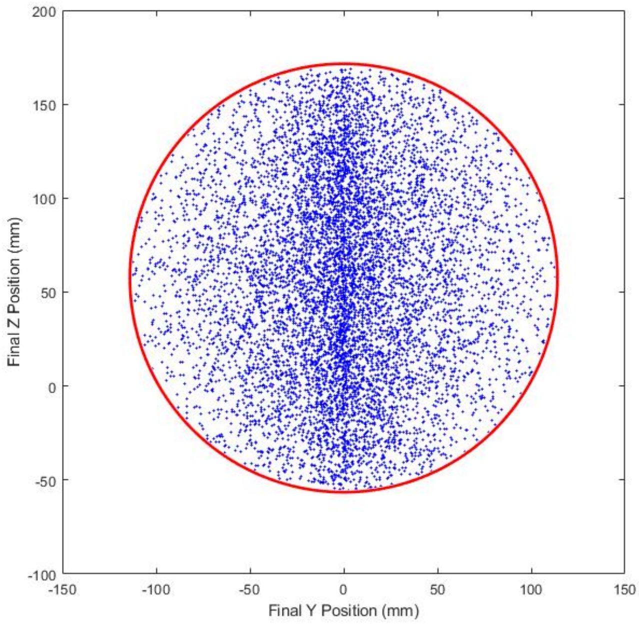

Figure 6.6: Print of a set of ions with azimuth and elevation "uniformly" distributed from $-90°$ to $90°$.

For this reasons, the results generated by a combination of two uniform distributions cannot be considered reliable for any kind of study, even the most basic one. Even if I cannot confirm the total validity of the other distributions, since they should be verified by tests that can simulate exactly the mentioned angular distributions, they can at least be considered physically consistent and thus reliable enough for the design and the performance estimation.

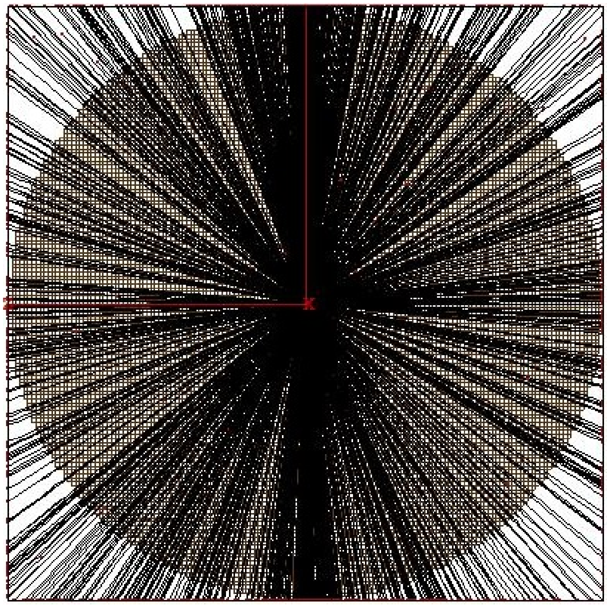

Figure 6.7: View from the plane YZ of a basic linear configuration. The particles are created with uniform distributions for both angles from -90° to 90°. A sort of "preference" exists for the y-axis.

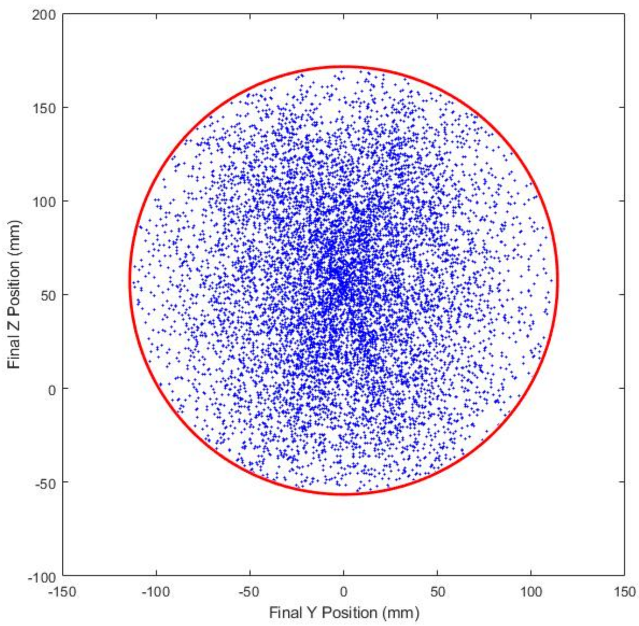

Figure 6.8: Print of a set of ions with azimuth and elevation "uniformly" distributed from -70° to 70°. The "vertical line" disappears but the pattern resembles a cross, like in Fig. 6.14.

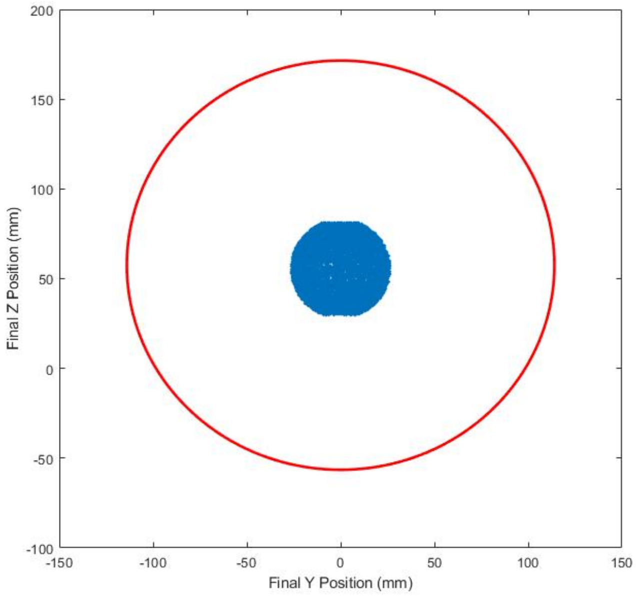

Figure 6.9: Print of a set of ions at 1 eV with azimuth and elevation ”uniformly” distributed from $-70°$ to $70°$.

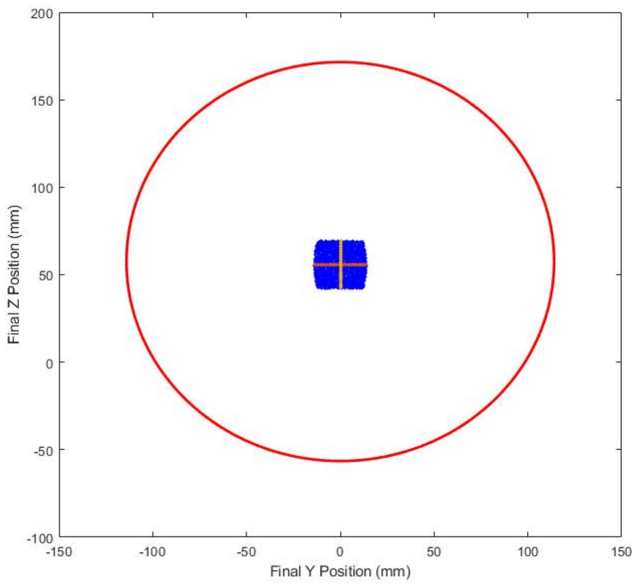

Figure 6.10: Print of a set of ions at 1 eV with azimuth and elevation ”uniformly” distributed from $-30°$ to $30°$. The red and yellow lines are the cases with respectively null elevation and null azimuth. The sizes of the two lines are the same as the blue distribution, so the coupling of the two angles has no particular effect here.

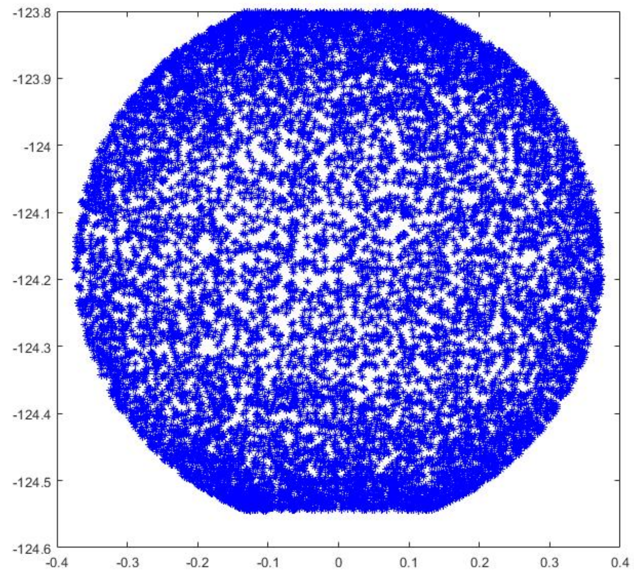

Figure 6.11: Print of a set of ions at 1 eV with azimuth and elevation "uniformly" distributed from -70° to 70° right after the ion generation.

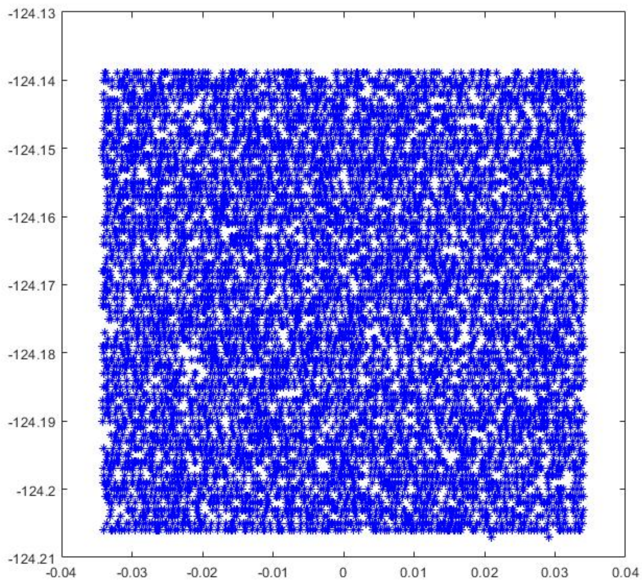

Figure 6.12: Print of a set of ions at 1 eV with azimuth and elevation "uniformly" distributed from -5° to 5° right after the ion generation.

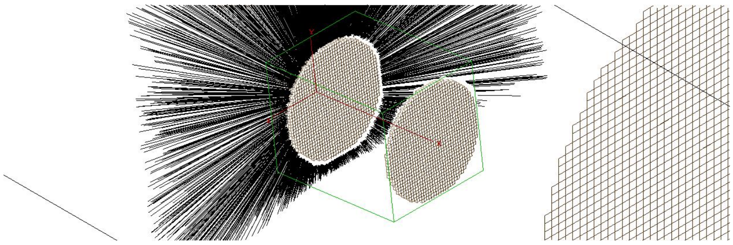

Figure 6.13: Isometric view of the ions generation from the target with azimuth and elevation ″uniformly″ distributed from −90° to 90° against the first acceleration grid.

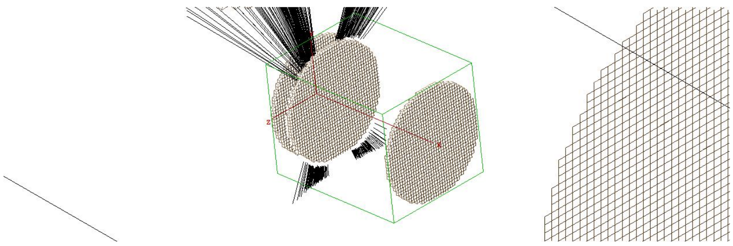

Figure 6.14: Isometric view of the ions generation from the target with azimuth and elevation ″uniformly″ distributed from −70° to 70° against the first acceleration grid.

Conclusions

This work proposes valid configurations for both a linear TOF Mass Spectrometer and a Reflectron. The next steps will be the CAD design of all the components and the supports, the order or manufacturing and in the end the construction of the instrument. Only at that point, after the calibration, the tests can start. Further optimization in the design is required according to the choice of the existing components, depending on the specifications and the costs.

The analysis in Chapter 6 is also meant as a sort of ”manual” of the instrument, so that the results of the experimental tests can be compared to the simulations in order to trace back the characteristics of the ions and get a more accurate understanding of the impact phenomenon. Thanks to these tests, the instrument can be further optimized or variations of it can be designed to study only certain features, as described in Chapter 4.

The main problem remains the separation of the effects of the initial energy and angular distributions on the spectra. The combination of the two proposed configurations can lead to an exact detection of them only in really special cases, with conditions hard to satisfy if in presence of an impact ionization. A more complex system with lenses or non-homogeneous fields, capable of increasing the order of focusing of the beam, is certainly desired for a deeper study. Much higher voltage levels are also welcome, because in this case the initial kinetic energy of the ions gets negligible (in our linear configuration the effect of initial energy on the total one could go up to 2%.).

The SIMION program can offer a valid help for the preliminary design but only being always careful to check if the final results are consistent with the initial conditions, as shown in Section 6.1. After the design and choice of the components, the CAD drawings can also be imported and inserted in the simulations in order to get more accurate results due to the non-ideal conditions of the system.

Appendix

Appendix A

Simion Instructions

The SIMION environment in which particles can be flown is a Workbench, so the first step is to create or load one.

The Workbench needs basically a set of Potential Arrays (.pa or .pa0), a Particle Definition (.fly, .fly2 or .ion), the Data Recording Definition (.rec), the Electrode Potentials (already inside the .iob) and the Potential Contours (.con). Some of them are necessary for the correct working (the Potential Arrays and the Particle Definition), the others are optional.

The particle definition defines the features of the ions that will be flown, that is to say the mass, the charge, the starting position, and so on; some of the values can be chosen as single values, others can be a sequence or a distribution.

The data recording definition defines the features of the ions that will be recorded and when they will be recorded, i.e. velocity and acceleration at the ion start and at its splat.

The potential arrays contain the geometry of every electrode, and at least one potential array for every single component should be created. The location of the potential arrays inside the Workbench is saved inside the Workbench itself. Usually potential arrays are created out of Geometry Files.

Geometry files are ASCII files where the geometry of one or more electrodes is coded. For ”How to create a GEM File”, please check the Manual.

HOW TO CREATE A WORKBENCH:

Open Simion 8.1 and click ’OK’ at the bottom right corner.

1) If a Potential Array (.pa0) already exists and has to be loaded, click ’Load’ under the Potential Arrays (PA) box. More PAs can be loaded at once. Jump to point 3).

2a) If instead a Potential Array has to be created, click ’New’: there a basic geometry can be designed using the various commands for symmetry, size, and so on.

2b) If a Potential Array has to be created out of a Geometry file, click on ’Use Geometry File (.GEM)...’ and choose the file .gem from your directory.

Once the Geometry File is loaded, the program goes back to the screen of point 1), and in the PA box we can see a new potential array: the name is the same of the geometry file, but the extension is ”.pa [*!]”. The geometry can still be modified by clicking on ’Modify’, both by using the commands on the screen or by editing the geometry file (’GeomF’ -> ’Edit...’): in this case, it’s always good to save the file, close it, click ’Compile’ to see if there are errors, and then ’Update PA’; at this point go back to the screen of point 1). When the geometry doesn’t need other variations, click ’Save’ and save the file with the extension ”.pa#”.

3) Click ’Refine’ to refine the geometry, if the parameters are correct click ’Refine’ again. If you loaded a PA (point 1) and it is already a .pa0, it doesn’t need refining but doing it doesn’t change anything. After refining, the file in the PA box will have the extension ”.pa0” and other files will be created in its folder depending on how many electrodes there are in the potential array.

4) Click ’Fast Adjust’ to set the potential on every electrode. This operation is not necessary, it can still be done while in the Workbench.

5) As stated in point 1), more PAs can be loaded in the same Workbench: for every PA that needs to be loaded, go back to 1); for every PA that needs to be created, go back to 2a) or 2b). When all the desired PAs are loaded or created, click 'View/Load Workbench'.

HOW TO FLY PARTICLES:

At this point a Workbench was loaded or created. In the second case, please click 'Save...' in the 'Workbench' tab.

6) Potential arrays might need a proper positioning. Click on the tab 'PAs': there you can choose the PAs in the "PA Instances" box and for each of them decide the potential on every electrode (by clicking 'Fast Adjust Voltages...' as in point 4) and/or change their scale or their location in the green "Positioning" box.

7) Particles have to be defined. Click on the 'Particles' tab and then on 'Define Particles...': here particles can be loaded, defined and saved. Please remember to check the 'Coordinates relative to' option, in order to start your particles from the correct point.

8) Staying in the 'Particles' tab it's possible to define the Data Recording Definition by clicking on 'Data Recording...': if the 'Record data' box is checked, data will be recorded in the 'Log' tab according the recording definition; if in addition in 'Output File:' a file name (i.e. .txt or .csv) is written, that file will be produced.

9) In the same tab, other options are available like the trajectory quality, the grouping of the ions, the colour of the trajectory, and so on.

10) In the tab 'PE/Contours', two functions are available for a better understanding: by clicking 'PE View', the current PA will be displayed in terms of potential energy, while in the blue 'Contours' zone, electric or magnetic field lines can be created

choosing number and colour.

11) Just above the displayed Workbench, the 'Display:' bar can be seen: with its buttons it's possible to change the plane of view and to print it.

12) When everything is set, click 'Fly'm' to fly the particles!

For a more accurate explanation please read the Manual, visit the website https://www.simion.com or check the Supplemental Documentation (open SIMION, click on the 'Help' tab, then 'Supplemental Documentation (Help)...').

Appendix B

Geometry File

Example of a basic 'geometry file' (.gem). The comments, that have to be erased in the actual file, are preceded by '%'.

```
pa_define(601,151) % define the maximum size of the array, at least
                   % 1 point greater than the measured size
locate(0)          % basic location of the system, '0' means the origin
{
e(1)               % electrode number 1, in this case the target
{
fill{within{box(0,0,10,150)}} % the 'fill' command takes the chosen shape
}                             % and fills it with whatever is explicited
e(2)                          % after ('within')
{
fill{within{box(120,0,120,150)}} % 'within' means that the shape will be
}                                % full; its counterpart is 'notin' that
e(3)                             % creates a hole
{
fill{within{box(480,0,480,150)}} % 'box' indicates a rectangular shape,
}                                % its coordinates are decided in the
e(4)                             % brackets
{
fill{within{box(580,0,580,150)}}
fill{within{box(580,0,590,61.8)}}
```

```
fill{within{box(590,0,600,150)}}
}
}

% the four numbers are the coordinates of the points of the rectangle:
% x0, y0, x1, y1; x0=x1 means that a grid of no x-size is created
```

Appendix C

Segmented MCP Measurements

Middle MCP with central hole							
	Radius (mm)	Radius (m)	sin(Θ)	Θ (°)	Difference (°)	Θ (center) (°)	Error (°)
Hole	2.00E+00	2.00E-03	4.00E-03	0.23			
First segment	5.17E+00	5.17E-03	1.03E-02	0.59	0.36	0.41	0.18
First Ring Gap	6.17E+00	6.17E-03	1.23E-02	0.71	0.11		
Second segment	9.33E+00	9.33E-03	1.87E-02	1.07	0.36	0.89	0.18
Second Ring Gap	1.03E+01	1.03E-02	2.07E-02	1.18	0.11		
Thrid segment	1.35E+01	1.35E-02	2.70E-02	1.55	0.36	1.37	0.18
MCP Width	1.00E+01	1.00E-02	2.00E-02	1.15	1.15		

The table collects all the measurements of the segmented MCP and the error committed in the ring gaps between the segments. 'sin(Θ)' is calculated as the Hole radius (m) divided by 0.5. 'Θ' is calculated as the 'arcsin' of the previous value. The 'Difference' is between every 'Θ' and the previous (upper) one. 'Θ (center)' is the sum of 'Θ' of the hole or the ring gaps and the 'Difference' of the segments. The 'Error' is the half of the 'Difference'.

Bibliography

[1] J. Dancer, "Destiny+ as a mission for dust astronomy." http://www.irs.uni-stuttgart.de/news/news_0145.html?__locale=en, 2018.

[2] JAXA, "Destiny+." https://sce.isas.jaxa.jp/destiny/wp-content/uploads/2018/07/cropped-D_image_180725.jpg.

[3] NASA, "Arecibo radar returns with asteroid phaethon images." https://www.jpl.nasa.gov/news/news.php?feature=7030.

[4] E. Grün, H. Fechtig, M. S. Hanner, J. Kissel, B. A. Lindblad, D. Linkert, D. Maas, G. E. Morfill, H. A. Zook, and R. H. Giese, "The galileo dust detector," *Space Sci. Rev. 60*, pp. 317–340, 1992.

[5] E. Grün, H. Fechtig, J. Kissel, D. Linkert, D. Maas, J. A. M. McDonnell, G. E. Morfill, G. Schehm, H. A. Zook, and R. H. Giese, "The ulysses dust experiment," *Astron. Astrophys. Suppl. Ser. 92*, pp. 411–423, 1992.

[6] E. Grün, B. Gustafson, I. Mann, M. Baghul, G. E. Morfill, P. Staubach, A. Taylor, and H. A. Zook, "Interstellar dust in the heliosphere," *Astron. Astrophys. 286*, pp. 915–924, 1994.

[7] H. Krüger, A. V. Krivov, and E. Grün, "A dust cloud of ganymede maintained by hypervelocity impacts of interplanetary micrometeoroids," *Planet. Space Sci. 48*, pp. 1457–1471, 2000.

[8] J. Kissel, D. E. Brownlee, K. Büchler, B. C. Clark, H. Fechtig, E. Grün, K. Hornung, E. B. Igenbergs, E. K. Jessberger, F. R. Krüger, H. Kuczera, J. A. M. McDonnell, G. M. Morfill, J. Rahe, G. H. Schwehm, Z. Sekanina, N. G. Utterback, H. J. Völk, and H. A. Zook, "Composition of comet halley dust particles from giotto observations," *Nature 321*, pp. 336–337, 1986.

[9] J. Kissel, R. Z. Sagdeev, J. L. Bertaux, V. N. Angarov, J. Audouze, J. E. Blamont, K. Büchler, E. N. Evlanov, H. Fechtig, M. N. Fomenkova, H. von Hoerner, N. A. Inogamov, V. N. Khromov, W. Knabe, F. R. Krüger, Y. Langevin, V. B. Leonas, A. C. Levasseur-Regourd, G. G. Managadze, S. N. Podkolzin, V. D. Shapiro, S. R. Tabaldyev, and B. V. Zubkov, "Composition of comet halley dust particles from vega observations," *Nature 321*, pp. 280–282, 1986.

[10] J. Kissel and F. R. Krüger, "The organic component in dust from comet halley as measured by the puma mass spectrometer on vega 1," *Nature 326*, pp. 755–760, 1987.

[11] M. Stübig, G. Schäfer, T.-M. Ho, R. Srama, and E. Grün, "Laboratory simulation improvements for hypervelocity micrometeorite impacts with a new dust particle source," *Planetary and Space Science 49*, pp. 853–858, 2001.

[12] S. Kempf, N. Altobelli, C. Briois, E. Grün, M. Horanyi, F. Postberg, J. Schmidt, R. Srama, Z. Sternovsky, G. Tobie, and M. Zolotov, "Suda: A dust mass spectrometer for compositional surface mapping for a mission to europa," *European Planetary Science Congress*, 2014.

[13] R. Srama, T. J. Ahrens, N. Altobelli, S. Auer, J. G. Bradley, M. Burton, V. V. Dikarev, T. Economou, H. Fechtig, M. Görlich, M. Grande, A. Graps, E. Grün, O. Havnes, S. Helfert, M. Horanyi, E. Igenbergs, E. K. Jessberger, T. V. Johnson, S. Kempf, A. V. Krivov, H. Krüger, A. Mocker-Ahlreep, G. Moragas-Klostermeyer, P. Lamy, M. Landgraf, D. Linkert, G. Linkert, F. Lura, J. A. M. Mcdonnell, D. Möhlmann, G. E. Morfill, M. Müller, M. Roy, G. Schäfer, G. Schlotzhauer, G. H. Schwehm, F. Spahn, M. Stübig, J. Svestka, V. Tschernjawski, A. J. Tuzzolino, R. Wäsch, and H. A. Zook, "The cassini cosmic dust analyzer," *Space Science Reviews*, 2004.

[14] NASA, "Cometary and interstellar dust analyser (cida)." https://stardust.jpl.nasa.gov/mission/cida.html, 2003.

[15] NASA, "Cosmic dust." https://curator.jsc.nasa.gov/dust/, August 2018.

[16] A. P. Jones, "Astrophysics of dust," *Astronomical Society of the Pacific Conference Series 309*, p. 347, 2004.

[17] S. T. Bromley, T. P. M. Goumans, E. Herbst, A. P. Jones, and B. Slater, "Challenges in modelling the reaction chemistry of interstellar dust," *Physical Chemistry Chemical Physics*, pp. 18607–19048, 2014.

[18] W. E. Stephens, "A pulsed mass spectrometer with time dispersion," *Proceedings of the American Physical Society 69*, p. 691, 1946.

[19] M. Krauss, "Chapter 15 - high resolution mass spectrometry in the effect-directed analysis of water resources," *Comprehensive Analytical Chemistry*, pp. 433–457, 2016.

[20] R. P. Schmid and C. Weickhardt, "Designing reflectron time-of-flight mass spectrometers with and without grids: a direct comparison," *International Journal of Mass Spectrometry*, vol. 206, no. 3, pp. 181–190, 2001.

[21] M. Yildirim, O. Sise, M. Dogan, and H. S. Kilic, "Designing multi-field linear time-of-flight mass spectrometers with higher-order space focusing," *International Journal of Mass Spectrometry*, vol. 291, no. 1-2, pp. 1–12, 2010.

[22] W. C. Wiley and I. H. Mc Laren, "Time of flight mass spectrometer with improved resolution," *Rev. Sci. Instrum. 26*, pp. 1150–1157, 1955.

[23] B. A. Mamyrin, V. I. Karataev, D. V. Shmikk, and V. A. Zagulin, "The mass-reflectron, a new nonmagnetic time-of-flight mass spectrometer with high resolution," *Sov. Phys. JETP 37*, pp. 45–51, 1973.

[24] W. P. Poschenrieder, "Multiple-focusing time-of-flight mass spectrometers. part ii. tofms with equal energy acceleration," *Int. J. Mass Spectrom. Ion Phys. 9*, pp. 357–373, 1972.

[25] T. Sakurai, T. Matsuo, and H. Matsuda, "Ion optics for time-of-flight mass spectrometers with multiple symmetry," *Int. J. Mass Spectrom. Ion Proc. 63*, pp. 273–287, 1985.

[26] J. H. J. Dawson and M. Guilhaus, "Orthogonal-acceleration time-of-flight mass spectrometer," *Rapid Commun. Mass Spectrom. 3*, pp. 1179–1185, 1989.

[27] T. Matsuo, M. Toyoda, T. Sakurai, and M. Ishihara, "Ion optics for multi-turn time-of-flight mass spectrometers with variable mass resolution," *J. Mass Spectrom. 32*, pp. 1179–1185, 1997.

[28] A. Mocker, K. Hornung, E. Grün, S. Kempf, A. Collette, K. Drake, M. Horányi, T. Munsat, L. O'Brien, Z. Sternovsky, and R. Srama, "On the application of a linear time-of-flight mass spectrometer for the investigation of hypervelocity impacts of micron and sub-micron sized dust particles," *Planetary and Space Science*, vol. 89, pp. 47–57, 2013.

[29] S. Kaesdorf, "Oft12 orthogonal extraction time-of-flight mass spectrometer." https://www.kaesdorf.de/OFT12.html.

[30] SCIEX, "Tripletof® 6600 system." https://sciex.com/products/mass-spectrometers/qtof-systems/tripletof-systems/tripletof-6600-system.

[31] IUAC, "Micro channel plate detector (mcp)." http://www.iuac.res.in/atmol/~safvan/mridulathesis/node21.html, 2014.

[32] I. JORDAN TOF PRODUCTS, "Time of flight components - mcp microchannel plate detectors." http://www.rmjordan.com/mcpdetector.html.

[33] T. Wien, "Basics of impact-ionization." http://www.iue.tuwien.ac.at/phd/triebl/node20.html.

[34] N. Lee, S. Close, D. Lauben, I. Linscott, A. Goel, T. Johnson, J. Yee, A. Fletcher, R. Srama, S. Bugiel, A. Mocker, P. Colestock, and S. Green, "Measurements of freely-expanding plasma from hypervelocity impacts," *International Journal of Impact Engineering*, pp. 40–49, 2012.

[35] SIMION, "Simion version 8.1." https://simion.com/.

[36] SIMION, "Lua." https://simion.com/info/lua.html.

[37] SIMION, "Quadrupole example." https://simion.com/info/examples.html.

[38] SIMION, "Sl tools tutorial." https://simion.com/info/sltoolstut.html.

[39] D. A. Dahl, T. R. McJunkin, and J. R. Scott, "Comparison of ion trajectories in vacuum and viscous environments using simion: insights for instrument design," *Int. J. Mass Spectrom. 266*, pp. 3875–3880, 2007.

[40] M. Guilhaus, "Principles and instrumentation in time-of-flight mass spectrometry: physical and instrumental concepts," *J. Mass Spectrom. 30*, pp. 1519–1532, 1995.

[41] K. P. Aicher, M. Müller, W. Ulf, and J. Grotemeyer, "Design and setup of an ion trap-reflectron-time-of-flight mass spectrometer," *Eur. Mass. Spectrom. 1*, pp. 331–340, 1995.

[42] A. Mocker, "Simulation of hyper-velocity dust impacts with ultra-short laser ablation." Grant Proposal, August 2014.

[43] V. M. Doroshenko and R. J. Cotter, "Ideal velocity focusing in a reflectron time-of-flight mass spectrometer," *Journal of the American Society for Mass Spectrometry*, vol. 10, no. 10, pp. 992–999, 1999.

[44] W. U. in St. Louis, "Reflectrons and ion mirrors." `https://msr.dom.wustl.edu/reflectrons-ion-mirrors/`.

[45] W. Contributors, "Reflectron." `https://en.wikipedia.org/wiki/Reflectron`, 2018.

[46] Y. Yoshida, November 1986. U.S. Patent 4,625,112,25.